Applicability and failure of the flux-gradient laws in double-diffusive convection

Timour Radko†

Department of Oceanography, Naval Postgraduate School, Monterey, CA 93943, USA

Double-diffusive flux-gradient laws are commonly used to describe the development of large-scale structures driven by salt fingers – thermohaline staircases, collective instability waves and intrusions. The flux-gradient model assumes that the vertical transport is uniquely determined by the local background temperature and salinity gradients. While flux-gradient laws adequately capture mixing characteristics on scales that greatly exceed those of primary double-diffusive instabilities, their accuracy rapidly deteriorates when the scale separation between primary and secondary instabilities is reduced. This study examines conditions for the breakdown of the flux-gradient laws using a combination of analytical arguments and direct numerical simulations. The applicability (failure) of the flux-gradient laws at large (small) scales is illustrated through the example of layering instability, which results in the spontaneous formation of thermohaline staircases from uniform temperature and salinity gradients. Our inquiry is focused on the properties of the 'point-of-failure' scale (H_{pof}) at which the vertical transport becomes significantly affected by the non-uniformity of the background stratification. It is hypothesized that H_{pof} can control some key characteristics of secondary double-diffusive phenomena, such as the thickness of high-gradient interfaces in thermohaline staircases. A more general parametrization of the vertical transport – the flux-gradient-aberrancy law – is proposed, which includes the selective damping of relatively short wavelengths that are inadequately represented by the flux-gradient models. The new formulation is free from the unphysical behaviour of the flux-gradient laws at small scales (e.g. the ultraviolet catastrophe) and can be readily implemented in theoretical and large-scale numerical models of double-diffusive convection.

Key words: convection, double diffusive convection

1. Introduction

Double-diffusive convection can be defined as a set of hydrodynamic phenomena related to the differences in molecular diffusivities of individual density components. For instance, in the oceanographic context, two major density components are temperature and salinity of seawater, and their diffusivities differ by two orders of magnitude. The primary double-diffusive instabilities – salt fingers and oscillatory diffusive perturbations – operate on the scale of molecular dissipation, which places

† Email address for correspondence: tradko@nps.edu

them into the category of microscale processes (~ 1 cm in the ocean). However, the vertical microscale mixing induced by double diffusion leads to the spontaneous generation of much larger structures: thermohaline intrusions, collective instabilities and layering modes. These fine-scale (~ 10 m vertically) phenomena, in turn, become active players in controlling the water-mass composition of the ocean, which makes it critical to elucidate their dynamics and transport characteristics. Comprehensive reviews of the subject are offered by Schmitt (1994, 2003) and Radko (2013).

Much of the progress in developing the fine-scale theory of double diffusion has resulted from the application of flux-gradient laws, which link the microstructure-driven fluxes of temperature and salinity to their local fine-scale gradients. Flux-gradient laws are often expressed in the form of Fick's diffusion model:

$$\begin{cases} F_T = -K_T \bar{T}_z, \\ F_S = -K_S \bar{S}_z, \end{cases} \tag{1.1}$$

where (F_T, F_S) are the fluxes of temperature (T) and salinity (S). The model assumes that the diffusivities (K_T, K_S) are uniquely determined by the fine-scale temperature and salinity gradients ($\bar{T}_z, \bar{S}_z$). Flux-gradient laws have been developed and used mostly for the fingering regime (e.g. Stern, Radko & Simeonov 2001; Stern & Simeonov 2002; Radko & Stern 2011), which is the main subject of the present study. While similar analyses for oscillatory diffusive convection are relatively rare, they also demonstrate the utility of flux-gradient modelling as a means of representing fine-scale dynamics (e.g. Mirouh *et al.* 2012).

Several problems have been successfully treated using flux-gradient laws, including theoretical investigations of thermohaline interleaving (Stern 1967; Merryfield 2000; Walsh & Ruddick 2000; Ruddick & Kerr 2003; Mueller, Smyth & Ruddick 2007; Smyth & Ruddick 2010), collective instability waves (Stern *et al.* 2001; Stern & Simeonov 2002; Radko & Stern 2011) and thermohaline staircases (Radko 2003; Stellmach *et al.* 2011). Attempts have also been made to validate the flux-gradient laws numerically (e.g. Stern *et al.* 2001; Stellmach *et al.* 2011) by comparing finger-resolving solutions with their parametric counterparts. These studies document the adequate performance of flux-gradient models in configurations characterized by the significant scale separation between salt fingers, which flux laws parametrize, and fine-scale phenomena, which are modelled using these laws. Unlike other forms of oceanic microstructure (convective or shear-driven turbulence), salt fingering is a narrow-band phenomenon operating on a well-defined heat dissipation scale (d). As long as the flux-gradient laws are applied to relatively large scales $L \gg d$, numerical evidence indicates that the resulting solutions are accurate and physical. A significant limitation of these analyses is that they describe purely double-diffusive phenomena. It should be realized that, in the oceanic environment, salt fingers interact with vertical shear and mechanically driven turbulence, which are seldom incorporated in the formulation of the flux-gradient laws.

Despite the apparent success in application of flux-gradient laws to large-scale phenomena, serious complications arise when the scale separation is limited. A case in point is the problem of spontaneous layering in an unbounded horizontally homogeneous and doubly stratified fluid (Radko 2003; Stellmach *et al.* 2011). Linear stability analysis of the parametrized mean-field equations reveals the existence of gamma-instability modes, which ultimately transform the uniform background gradient into a series of mixed layers separated by high-gradient interfaces. The parametric flux-gradient model predicts that the growth rate of the unstable gamma-modes

monotonically increases without bound with increasing vertical wavenumber, which is clearly unphysical. This ultraviolet catastrophe in the parametric model also contradicts the direct numerical simulations (DNS) showing that the wavelength of the fastest-growing gamma-instability mode exceeds the salt-finger scale by more than an order of magnitude (Radko 2003; Stellmach *et al.* 2011). This apparent discrepancy signals that the flux-gradient laws fail at relatively small scales. As a result of this failure, the parametric model cannot predict the fundamental characteristics of thermohaline staircases, such as the initial layer heights or the thicknesses of high-gradient interfaces (e.g. Radko 2005). These deficiencies underscore the need to quantify the applicability range of the flux-gradient laws and to suggest alternative parametrizations for moderately small scales.

Unfortunately, the flux-gradient laws themselves provide no guidance with regard to their range of validity, and our insight into the specific conditions that set the point-of-failure scale is limited. Aside from a few DNS-based attempts to assess the accuracy of the flux-gradient laws at various scales (e.g. Traxler *et al.* 2011), the general theory for their applicability is notably missing. The development of such a theory from first principles is one of the main objectives of this study. The proposed model is based on the techniques of multiscale analysis (reviewed most recently by Mei & Vernescu (2010)), which allow explicit representation of the interaction between small and large scales of motion. This transparency is exploited here to conceptualize the point-of-failure effect – the loss of fidelity of flux-gradient laws at small vertical scales. The problem of spontaneous layering in the initially uniform finger-favourable stratification is examined using an asymptotic expansion in which the small parameter ε measures the ratio of the primary (finger) scales and those of larger layering modes.

In our study, the explicit asymptotic ($\varepsilon \to 0$) multiscale solutions representing the layering modes are compared to their finite-amplitude counterparts. The substantial deviation of the two solutions at relatively short wavelengths is interpreted as a sign that the lack of scale separation (i.e. finite ε) is affecting the large-scale dynamics. In this regime, the relevance of flux-gradient models becomes questionable. Therefore, the difference between asymptotic and finite-amplitude solutions is used as a criterion for the applicability or failure of the flux-gradient laws, ultimately resulting in an explicit model for the point-of-failure scale (H_{pof}). The finite-ε solutions also offer important insights into the mechanics of the flux-law failure. They suggest that the system of vertically elongated fingers is stable with respect to horizontally uniform perturbations as long as the vertical scale of these perturbations is small ($H < H_{pof}$), which explains the damping of short wavelengths observed in DNS. Since flux-gradient laws do not explicitly represent the details of microscale dynamics, it is not surprising that they fail to capture the small-scale stabilization effect and suffer from unphysical behaviours.

Incidentally, the complications related to the failure of the flux-gradient laws at small scales are not limited to double diffusion. Earlier attempts to represent turbulence in one-component flows (Phillips 1972; Posmentier 1977) by the flux-gradient model also reveal analogous dynamics at small scales, ultimately resulting in the ultraviolet catastrophe (Ruddick *et al.* 1989). However, we will argue that the specific mechanisms responsible for the failure of flux laws in double-diffusive and one-component flows might be substantially different.

This paper is organized as follows. Section 2 reviews the flux-gradient model of spontaneous layering in uniform finger-favourable background stratification. We examine a series of DNS, which demonstrate that the flux-gradient model adequately represents the layering instability for relatively large scales but fails when the scale

separation between the layering modes and salt fingers becomes less pronounced. Section 3 presents an alternative view of double-diffusive layering afforded by the multiscale model and discusses direct analogies that exist between multiscale and flux-gradient formulations. In §4, we identify conditions for the breakdown of the multiscale expansion, develop an analytical model for the point-of-failure scale, and then (§5) test our theory by DNS. To correct the unphysical behaviour of the flux-gradient laws at small scales, we propose their adjustment (§6), which takes into account the selective damping of short waves. We examine parametric solutions based on the proposed flux laws and demonstrate that the point-of-failure scale controls several essential characteristics of double-diffusive convection, such as the thickness of salt-finger interfaces in fully developed thermohaline staircases. In §7, we draw conclusions and summarize our findings.

2. Preliminary considerations

2.1. *Formulation*

Following the conventional treatment of double-diffusive problems (e.g. Stern *et al.* 2001), the temperature and salinity fields are separated into the basic state $(\bar{\bar{T}}, \bar{\bar{S}})$, representing a uniform vertical gradient, and a departure (T, S) from it. Our focus is on finger-favourable background stratification $(\bar{\bar{T}}_z > 0, \ \bar{\bar{S}}_z > 0)$. The governing Boussinesq equations of motion are expressed in terms of perturbations T and S. To reduce the number of controlling parameters, the system is non-dimensionalized, using $l = (k_T \nu / g \alpha \bar{\bar{T}}_z)^{1/4}$, k_T/l, l^2/k_T and $\rho_0 \nu k_T / l^2$ as the scales of length, velocity, time and pressure respectively. Here, (k_T, k_S) denote the molecular diffusivities of heat and salt, and ρ_0 is the reference density used in the Boussinesq approximation. The expansion/contraction coefficients (α, β) are incorporated in (T, S), and $\alpha \bar{\bar{T}}_z l$ is used as the scale for both temperature and salinity perturbations. As a result, the governing equations reduce to

$$
\begin{cases}
\dfrac{\partial T}{\partial t} + \boldsymbol{v} \cdot \boldsymbol{\nabla} T + w = \nabla^2 T, \\[2mm]
\dfrac{\partial S}{\partial t} + \boldsymbol{v} \cdot \boldsymbol{\nabla} S + \dfrac{w}{\bar{\bar{R}}_\rho} = \tau \nabla^2 S, \\[2mm]
\dfrac{1}{Pr} \left(\dfrac{\partial}{\partial t} \boldsymbol{v} + \boldsymbol{v} \cdot \boldsymbol{\nabla} \boldsymbol{v} \right) = -\boldsymbol{\nabla} p + (T - S)\boldsymbol{k} + \nabla^2 \boldsymbol{v}, \\[2mm]
\boldsymbol{\nabla} \cdot \boldsymbol{v} = 0,
\end{cases}
\tag{2.1}
$$

where $\bar{\bar{R}}_\rho = \alpha \bar{\bar{T}}_{z,dim} / \beta \bar{\bar{S}}_{z,dim}$ is the background density ratio (the subscript *dim* hereafter denotes dimensional quantities), $\tau = k_S/k_T$ is the diffusivity ratio, $Pr = \nu/k_T$ is the Prandtl number, $\boldsymbol{v} = (u, v, w)$ is the velocity vector and $\boldsymbol{k}$ is the vertical unit vector. Much of the discussion in this study concerns the dynamics of fine-scale flow components, operating on scales greatly exceeding the typical size of individual fingers. These fine-scale quantities will be indicated using single overbars. For quantitative analyses of simulations in this paper, we use a more specific operational definition of $(\bar{T}, \bar{S}, \bar{\boldsymbol{v}})$ as the horizontal averages across the model domain.

The non-dimensional formulation (2.1) suggests that, for a given fluid, the evolution of double-diffusive systems is largely controlled by the density ratio. Therefore, double-diffusive theory ascribes the utmost significance to the ratio of the

background gradients of temperature and salinity, rather than to their individual values. Accordingly, the vertical diffusivities used in the formulation of the flux-gradient laws (1.1), both dimensional and non-dimensional, are often assumed to be uniquely determined by the fine-scale density ratio $\bar{R}_\rho = \bar{T}_z / \bar{S}_z$:

$$\begin{cases} K_{T,dim} = K_T(\bar{R}_\rho) k_T, \\ K_{S,dim} = K_S(\bar{R}_\rho) k_T. \end{cases} \tag{2.2}$$

The assumed form (2.2) of the flux laws appears to be relevant and physical for configurations where the spatial variability in mean gradients is limited to long wavelengths, which greatly exceed the nominal salt-finger scale. In such gently varying systems, the mean patterns $(\bar{T}, \bar{S})$ can be locally approximated by the corresponding linear gradients $(\bar{\bar{T}}, \bar{\bar{S}})$. This suggests, in light of (2.1), that the key transport characteristics are determined by $\bar{R}_\rho \approx \bar{\bar{R}}_\rho$. However, this physical argument may not be applicable to relatively small-scale phenomena, where the spatial extent of stratification non-uniformity is comparable to the finger scale.

In addition to the governing equations (2.1), which are relevant for all spatial and temporal scales, we also consider the one-dimensional (z) parametric model, which describes the evolution of mean components $(\bar{T}, \bar{S})$. This parametric system is based on the flux-gradient laws (1.1) and assumes that the vertical diffusivities are uniquely determined by the local fine-scale density ratio as indicated in (2.2). Of particular interest in our investigation are the conditions for its applicability and failure. In terms of our non-dimensional units, it reduces (e.g. Radko 2003; Traxler *et al.* 2011) to

$$\begin{cases} \dfrac{\partial \bar{T}}{\partial t} = -\dfrac{\partial}{\partial z} F_T = \dfrac{\partial}{\partial z}\left(K_T(\bar{R}_\rho)\dfrac{\partial \bar{T}}{\partial z}\right) = \dfrac{\partial}{\partial z}\left(Nu\dfrac{\partial \bar{T}}{\partial z}\right), \\ \dfrac{\partial \bar{S}}{\partial t} = -\dfrac{\partial}{\partial z} F_S = \dfrac{\partial}{\partial z}\left(K_S(\bar{R}_\rho)\dfrac{\partial \bar{S}}{\partial z}\right) = \dfrac{\partial}{\partial z}\left(\dfrac{Nu}{\gamma}\dfrac{\partial \bar{T}}{\partial z}\right), \end{cases} \tag{2.3}$$

where $Nu = K_T = K_{T,dim}/k_T$ is the Nusselt number and $\gamma = \alpha F_{T,dim}/\beta F_{S,dim} = F_T/F_S = K_T \bar{R}_\rho / K_S$ is the flux ratio, both of which are assumed to be uniquely determined by the fine-scale density ratio. We emphasize, however, that the aforementioned problem of flux-law failure is not caused by this, rather conventional, assumption. Even if the diffusivities of flux-gradient laws were instead expressed as functions of individual mean gradients $K_{T,S} = K_{T,S}(\bar{T}_z, \bar{S}_z)$, these laws would still exhibit the same unphysical behaviour at small scales. Therefore, we focus our inquiry on the failure conditions of the simpler system (2.3).

While the R_ρ-dependent form of vertical diffusivities in (2.2) and flux laws in (2.3) is widely accepted and heavily used in all branches of double diffusion, questions could be raised with regard to their generality. In particular, it is implicit in the governing equations (2.1) that double-diffusive transport may also be sensitive to the spatial scales of the mean T–S gradients. Examining the conditions and ramifications of the failure of the flux-gradient laws is the major objective of our study.

2.2. *Instability of the flux-gradient laws*

In order to assess the merits and limitations of the parametric system (2.3), we first review its linear stability properties (Walsh & Ruddick 2000; Radko 2003). The net fine-scale stratification $(\bar{T}, \bar{S})$ is therefore separated into the linear background
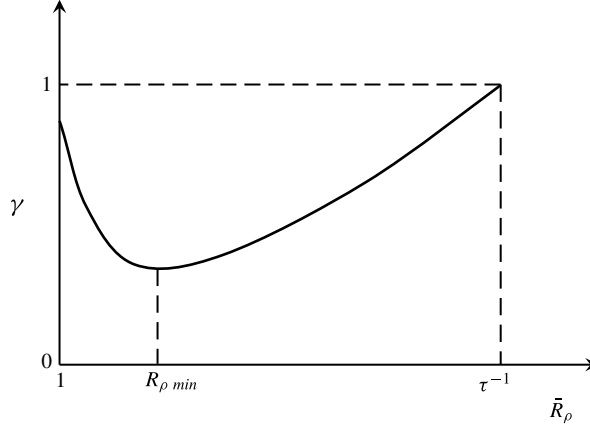
FIGURE 1. Dependence of the flux ratio (γ) on the density ratio (R_ρ).

gradients $(\bar{\bar{T}}, \bar{\bar{S}})$ and the weak perturbation (T_f, S_f). The parametric system is then linearized for $(T_f, S_f) \ll 1$ and its stability is analysed using normal modes $(T_f, S_f) = (\hat{T}, \hat{S}) \exp(\mathrm{i}mz + \lambda t)$, which results in the growth-rate equation

$$\left(\frac{\lambda}{m^2}\right)^2 + \left(\frac{\lambda}{m^2}\right) \left(A_{Nu} + Nu(\bar{\bar{R}}_\rho) - A_\gamma Nu(\bar{\bar{R}}_\rho)\bar{\bar{R}}_\rho - \frac{\bar{\bar{R}}_\rho A_{Nu}}{\gamma(\bar{\bar{R}}_\rho)}\right) - A_\gamma Nu^2(\bar{\bar{R}}_\rho)\bar{\bar{R}}_\rho = 0,$$
(2.4)

where

$$A_{Nu} = \bar{\bar{R}}_\rho \left.\frac{\partial Nu}{\partial \bar{R}_\rho}\right|_{\bar{R}_\rho = \bar{\bar{R}}_\rho} \quad \text{and} \quad A_\gamma = \bar{\bar{R}}_\rho \left.\frac{\partial \gamma^{-1}}{\partial \bar{R}_\rho}\right|_{\bar{R}_\rho = \bar{\bar{R}}_\rho}. \tag{2.5a,b}$$

The form of the growth-rate equation indicates that the stability of perturbations does not depend on their vertical scale. A decrease in the vertical scale (larger m) increases the magnitude of the growth rate, but does not change the sign of $\mathrm{Re}(\lambda)$. The normalized growth rate $\lambda_{norm} = \lambda/m^2$, and hence the stability or instability of our system, is determined by the coefficients of (2.4) and, ultimately, by the background density ratio $\bar{\bar{R}}_\rho$.

Particularly significant is the sign of A_γ. Theoretical arguments and numerical simulations (Schmitt 1979*a*,*b*; Radko 2003; Stellmach *et al.* 2011) indicate that the $\gamma(\bar{R}_\rho)$ dependence is non-monotonic. As the density ratio increases from unity, the flux ratio first decreases, as shown in figure 1, reaches a minimum value (at $\bar{R}_\rho = R_{\rho,min}$) and then starts to increase. For the background density ratios in the range $1 < \bar{\bar{R}}_\rho < R_{\rho,min}$, the free coefficient of the quadratic equation is negative ($A_\gamma > 0$), which implies that there are two real roots of opposite sign. The existence of a positive root means that the basic uniform gradient is unstable. It can also be shown that, under certain unrestrictive assumptions, the flux-gradient laws are stable for $\bar{\bar{R}}_\rho > R_{\rho,min}$.

The reason why the uniform gradient is stable for some values of $\bar{\bar{R}}_\rho$ but unstable for others becomes more apparent from inspection of the parametric density equation, which is readily obtained by subtracting S and T equations in the flux-gradient
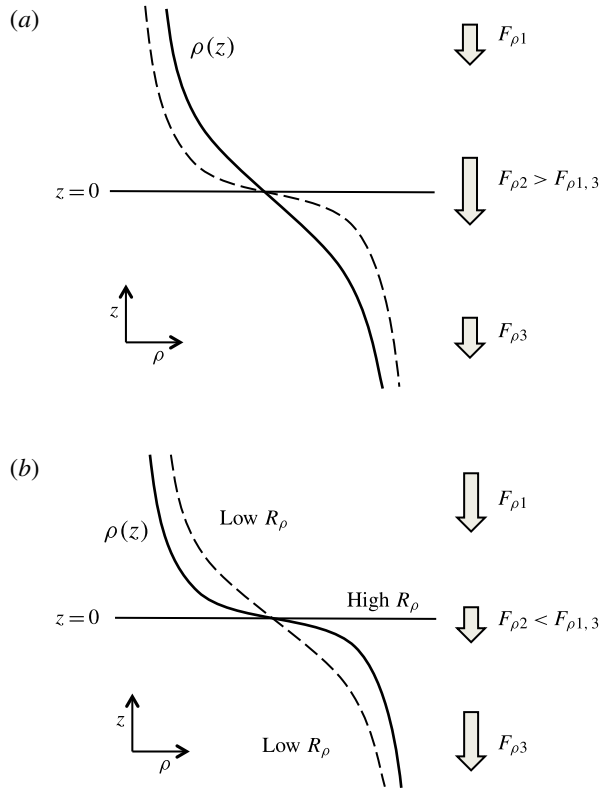
FIGURE 2. Schematics illustrating the stability properties of a uniform finger-favourable stratification. (*a*) The destabilizing tendency due to negative diffusivity of density. (*b*) The stabilizing effect of variable R_ρ-dependent diffusivity.

form (2.3):

$$\frac{\partial \bar{\rho}}{\partial t} = \frac{\partial}{\partial z}\left(K_\rho \frac{\partial \bar{\rho}}{\partial z}\right) = K_\rho \frac{\partial^2 \bar{\rho}}{\partial z^2} + \frac{\partial K_\rho}{\partial \bar{R}_\rho} \frac{\partial \bar{R}_\rho}{\partial z} \frac{\partial \bar{\rho}}{\partial z}. \tag{2.6}$$

The diffusivity of density K_ρ in (2.6) is related to (K_T, K_S) as follows:

$$K_\rho = \frac{K_T(\bar{R}_\rho)\bar{R}_\rho - K_S(\bar{R}_\rho)}{\bar{R}_\rho - 1}, \tag{2.7}$$

which implies that K_ρ is uniquely determined by the fine-scale density ratio. Equation (2.6) indicates that the growth or decay of small-amplitude perturbations to the uniform stratification is controlled by the competition between adverse effects represented by the two terms on its right-hand side. The diffusive term $K_\rho \partial^2 \bar{\rho}/\partial z^2$ is always destabilizing. Double diffusion is driven by the release of potential energy from the background stratification – the light upper part of the water column becomes lighter, and the heavy lower part becomes even heavier. Therefore, the eddy diffusivity of density (K_ρ) is negative, which should have a destabilizing effect on smoothly stratified regions of the ocean (e.g. Schmitt 1994). The physical reasons are illustrated in figure 2(*a*). Consider a perturbation to the uniform density stratification (solid curve), which locally increases the density gradient at $z = 0$. If the density ratio

plays a lesser role than the density gradient in terms of controlling variability of the vertical density flux $(-K_\rho \, \partial\bar{\rho}/\partial z)$, then the downward density flux at $z = 0$ $(F_{\rho 2})$ would tend to exceed that in the regions above $(F_{\rho 1})$ and below $(F_{\rho 3})$. The associated flux divergence patterns result in a density decrease (increase) in the $z > 0$ $(z < 0)$ region, which reinforces the original perturbation, as indicated in figure 2(*a*). This instability is expected ultimately to produce the step-like stratification suggestive of oceanic thermohaline staircases.

The origin of the negative-diffusivity hypothesis can be traced to the heuristic arguments put forward by Phillips (1972) and Posmentier (1977) for one-component turbulent fluids. In the Phillips–Posmentier model, the density equation – the counterpart of (2.6) – takes the following form:

$$\frac{\partial}{\partial t} \bar{\rho}^{PP} = -\frac{\partial}{\partial z} F_{\rho}^{PP}(\bar{\rho}_z^{PP}) = -\frac{\partial F_{\rho}^{PP}}{\partial \bar{\rho}_z^{PP}} \bar{\rho}_{zz}^{PP}, \tag{2.8}$$

where superscript *PP* refers to the Phillips–Posmentier formulation. The vertical flux is assumed to be determined by the density gradient and (2.8) is expected to produce unstable solutions as long as $\partial F_{\rho}^{PP}/\partial \bar{\rho}_z^{PP} > 0$. The physical parallels of this idea with the negative-diffusivity mechanism for double diffusion are apparent. In both cases, the instability is triggered by variation in vertical transport with the density gradient. A significant caveat in this analogy is that the density flux in one-component turbulent fluids is generally directed upwards, whereas the double-diffusive flux is downwards. Nevertheless, both systems produce similar flux convergence patterns in response to changes in density stratification, and the dynamical illustration of the anti-diffusive mechanism (figure 2*a*) can be readily adapted for the Phillips–Posmentier configuration. Given the destabilizing tendency of negative-density diffusion in (2.6), the explanations based on the Phillips–Posmentier paradigm at first glance come across as a good fit to the thermohaline layering problem.

The major concern with regard to the negative-diffusivity mechanism is that staircases in the finger-favourable regions of the world's oceans are not very common. Even in the controlled setting of laboratory experiments, fingering convection often maintains smooth vertical stratification (e.g. Krishnamurti 2003). These observations suggest the existence of some dynamic process capable of neutralizing the destabilizing tendency of the negative-diffusivity effect. The likely candidate is the variation of density diffusivity with $\bar{R}_\rho$, represented by the second term on the right-hand side of (2.6). The mechanics of the variable-density-ratio effect is illustrated in figure 2(*b*), which shows a perturbation to the uniform density stratification (solid curve) that locally increases the density ratio at $z = 0$. In regions above and below this level, the density ratio is lower, and therefore the temperature and salinity gradients are more density-compensated. Thus, density is relatively homogeneous in $z < 0$ and $z > 0$ regions but stratified at $z \approx 0$. Note that the intensity of double diffusion rapidly decreases with increasing $\bar{R}_\rho$, as does $|K_\rho|$. Thus, if the density ratio plays a greater role than the density gradient in terms of controlling the vertical density flux $(-K_\rho \, \partial\bar{\rho}/\partial z)$, then the downward density flux would be less at $z = 0$ $(F_{\rho 2})$ than in the regions above $(F_{\rho 1})$ and below $(F_{\rho 3})$. As a result, the initially step-like distribution gradually relaxes towards the linear background stratification, as indicated in figure 2(*b*). The winner of the competition between the (destabilizing) negative-diffusivity and (stabilizing) variable-diffusivity mechanisms is ultimately determined by the background density ratio. Salt-finger staircases generally tend to form in the ocean for relatively low density ratios ($\bar{\bar{R}}_\rho \leqslant 1.7$), for which the

negative-diffusivity effect is expected to dominate. Our subsequent analyses will be focused on this layering-favourable parameter range.

The foregoing discussion draws attention to the potential risks that are inherent in the widespread attempts (e.g. Schmitt 1994; Ruddick 1997; Kelley *et al.* 2003) to adopt the one-component Phillips–Posmentier conceptualization to double-diffusive layering. The Phillips–Posmentier model captures only one aspect of the problem – the ρ_z effect (figure 2*a*). The second key dynamical element – the R_ρ effect (figure 2*b*) – is fundamentally double-diffusive and has no counterpart in one-component systems. It acts against the ρ_z effect and can easily control the evolution of double-diffusive systems for typical oceanic conditions. Therefore any physical analysis of thermohaline layering has to explore both degrees of freedom in double-diffusive systems – $\bar{T}_z$ and $\bar{S}_z$ or, equivalently, $\bar{\rho}_z$ and $\bar{R}_\rho$.

2.3. *The point-of-failure scale*

In order to test the parametric flux-gradient theory and, in particular, to quantify its range of validity, we first turn to DNS. Layering DNS still represent a considerable computational challenge, particularly in the oceanographic (heat–salt) context. The key difficulty is the wide range of spatial and temporal scales that require adequate resolution. The scale of salt dissipation is less than the scale of heat dissipation by a factor of $\tau^{-0.5} \sim 10$ and the scale of heat dissipation is, in turn, much less than the typical step height in the staircase. These computational constraints place three-dimensional (3D) layering DNS for the heat–salt parameters beyond the reach of modern computers. Numerical modellers have two options: either to compromise on the governing parameters, using a diffusivity ratio that is higher than the heat–salt value, or to resort to two-dimensional (2D) simulations. On a positive note, neither approach leads to qualitative inconsistencies. As discussed in Stern *et al.* (2001) and Radko (2008), the use of a moderate diffusivity ratio is not expected to alter the fundamental physics of salt fingering, as long as τ remains significantly less than unity. The 3D simulations tend to elevate vertical fluxes by a factor of 2 or so relative to the corresponding 2D simulations. However, on the qualitative level, all major double-diffusive phenomena appear to be adequately represented by 2D models.

In this study we pursue both approaches. We use 2D simulations to focus directly on the oceanographically relevant parameters $(Pr, \tau) = (7, 0.01)$. To ensure that our conclusions are not compromised by neglecting fundamentally 3D effects, we supplement our 2D simulations by 3D runs in a computationally accessible regime ($\tau = 0.1$). We assume periodic boundary conditions in each spatial direction and integrate the governing equations (2.1) using the dealiased pseudospectral method (e.g. Stern *et al.* 2001; Stellmach *et al.* 2011). The accuracy of simulations in this study was ascertained by reproducing selected runs with doubled spatial resolution, which resulted in minimal (3 % or less) changes in the equilibrium *T*–*S* fluxes. Inspection of the salinity variance spectra confirmed that the salt dissipation scale is fully resolved.

Each of the following experiments has been initiated by the state at rest, perturbed by the small-amplitude fundamental harmonic

$$(T_1, S_1) = (A_{T0}, A_{S0}) \sin(2\pi z/H), \tag{2.9}$$

where H is the vertical extent of the computational domain. The amplitude of this harmonic (A_T, A_S) was recorded throughout the experiment, and its variation in time was used to infer the growth rate of layering instability.
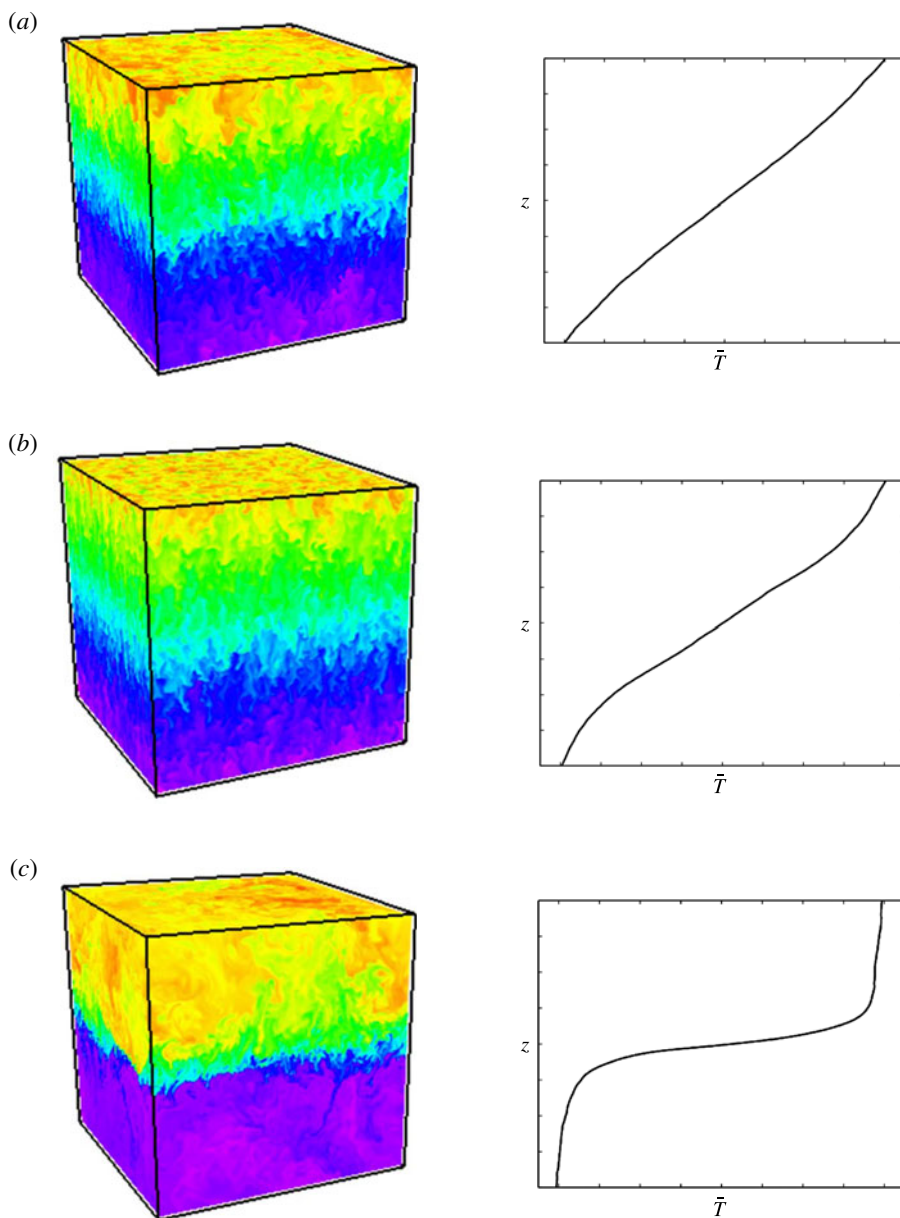
FIGURE 3. (Colour online) Three-dimensional DNS of fingering convection. The instantaneous temperature fields are shown at various times in the left panels and the horizontally averaged temperature profiles are on the right. The experiment is performed for $\bar{\bar{R}}_\rho = 1.1$ and the vertical extent of the domain is $H = 400$.

Figures 3 and 4 present some typical 3D experiments performed for the numerically accessible parameters $(Pr, \tau, \bar{\bar{R}}_\rho) = (7, 0.1, 1.1)$. The first simulation (figure 3) was carried out in the computational domain of size $400 \times 400 \times 400$, which, assuming stratification typical for the mid-latitude thermocline, corresponds to dimensional values of 4 m $\times$ 4 m $\times$ 4 m. The evolutionary pattern is illustrated in a sequence of
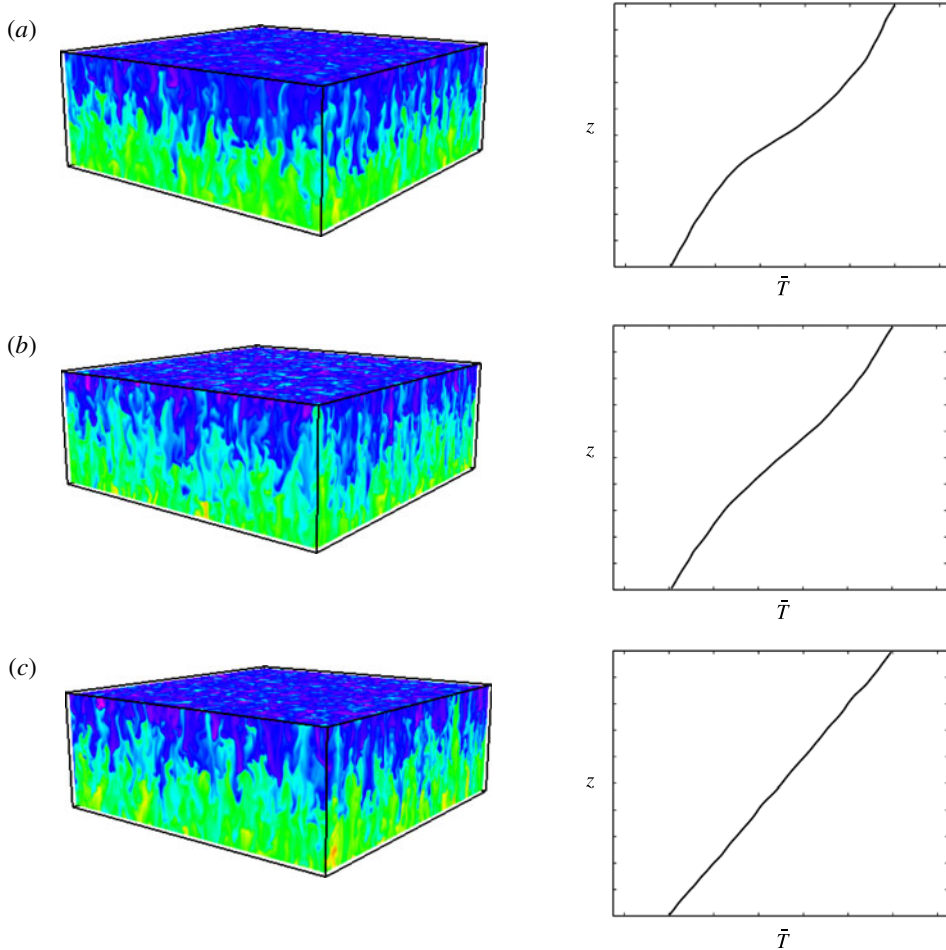
FIGURE 4. (Colour online) The same as in figure 4, but the vertical extent is $H = 150$. The change in H alters the stability properties of the system.

temperature snapshots (left panels) and the corresponding horizontally averaged total temperature profiles $\bar{T}(z)$ (right panels) for $t = 44$, 143 and 255 (figure 3a–c). This experiment revealed that the initially introduced fundamental harmonic perturbation grows monotonically, at a rate consistent with the prediction of the gamma-instability theory (2.4), and ultimately transforms the initial stratification into a well-defined two-layer system. The simulation in figure 4 is identical to that in figure 3, except that the vertical scale is reduced to $H = 150$. However, the outcome of this experiment is dramatically different – the system does not evolve into the two-layer configuration. Instead, the initially introduced perturbation gradually decreases and the system relaxes to the linear background stratification. This result directly contradicts the flux-gradient model (2.4), which predicts that the growth rate should increase with the increasing perturbation wavenumber $m = 2\pi/H$.

The effects revealed by 3D simulations are also realized very clearly in two dimensions. The 2D simulations carry an obvious benefit of numerical efficiency, which allows us to use the oceanographically relevant diffusivity ratio (τ) and affords a more complete exploration of the parameter space (R_ρ, H). It should also be noted
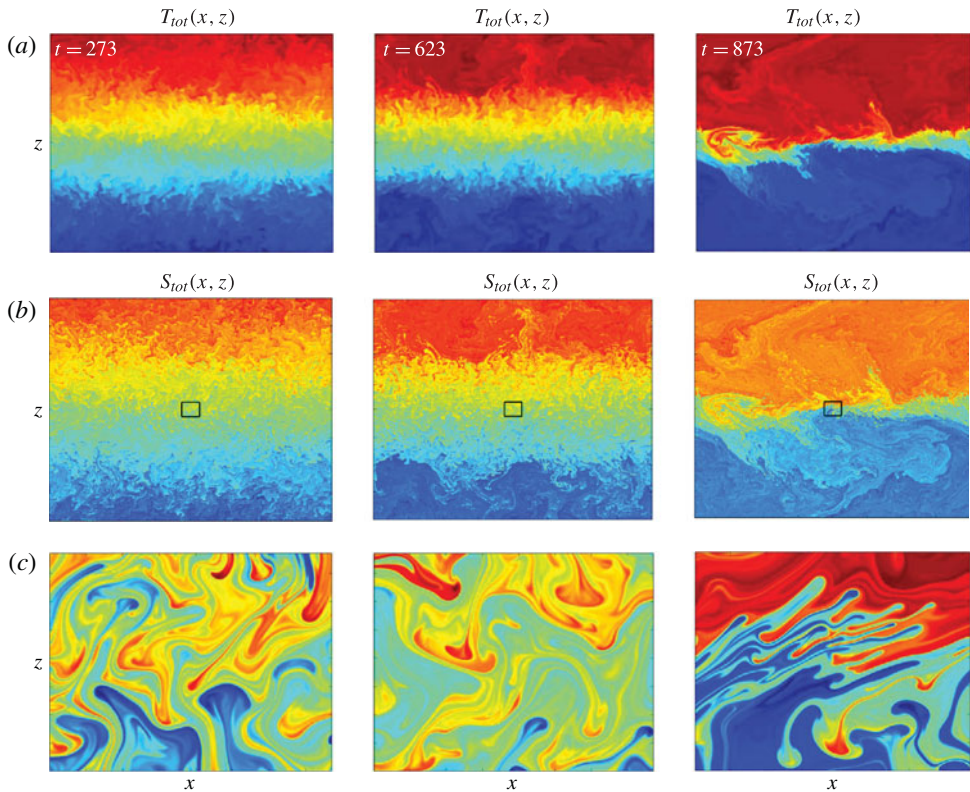
FIGURE 5. (Colour online) Two-dimensional DNS. The experiment is performed for $\bar{\bar{R}}_\rho = 1.5$ and $H = 400$. (*a*) The instantaneous temperature fields at various times. (*b*) The corresponding salinity fields. (*c*) Enlarged views of the square areas marked in (*b*).

that sheared environments favour formation of salt sheets aligned in the direction of the background shear (Linden 1974; Kimura & Smyth 2007), in which case salt-finger dynamics become effectively 2D. It is perhaps ironic that, since large-scale shears are ubiquitous in the ocean, salt fingers may be better represented by 2D than by 3D simulations.

Figure 5 presents a typical 2D simulation in the unstable regime. The governing parameters are $(R_\rho, Pr, \tau) = (1.5, 7, 0.01)$, the domain size is 400×400 and the numerical mesh contains $(N_x, N_z) = (6144, 6144)$ grid points. Figure 5 illustrates the wide range of dynamically active scales in fingering convection and the associated numerical complications. The salinity texture (panels *b*) contains much finer scales than the corresponding temperature patterns (panels *a*). The requirement to resolve these minute salinity filaments (enlarged views of which are shown in panels *c*) dramatically increases the computational expense of fingering simulations and precludes 3D simulations in the same parameter range as shown in figure 5.

As expected from flux-gradient theory, the initially introduced perturbation (2.9) grows exponentially and eventually transforms the flow pattern into a system consisting of two well-mixed layers separated by a thin high-gradient interface (figure 5). To provide a quantitative comparison between DNS and the flux-gradient theory, the numerical growth rate was computed from the best exponential fit to the

temperature amplitude record $A_T(t)$ of the fundamental harmonic:

$$A_{fit}(t) = A_{fit}(0) + \hat{A}[\exp(\lambda_{num}t) - 1].$$ (2.10)

The growth rate estimated from the fit (2.10) for the experiment in figure 5 is

$$\lambda_{num} = 1.664 \times 10^{-3},$$ (2.11)

representing a dimensional amplification time scale of approximately one week.

To evaluate the corresponding theoretical prediction (λ_{theor}), we use the growth-rate equation (2.4). The coefficients of (2.4) have been determined through a series of DNS, simulating salt fingers in uniform gradients for density ratios in the range $1.15 < \bar{\bar{R}}_\rho < 1.95$. It was found that the equilibrium fluxes in these simulations can be closely approximated by the following analytical expressions:

$$\begin{cases} F_S \approx \dfrac{a_S}{\sqrt{\bar{\bar{R}}_\rho - 1}} + b_S, & (a_S, b_S) = (136.9, -105.13), \\ \gamma \approx a_\gamma \exp(b_\gamma \bar{\bar{R}}_\rho) + c_\gamma, & (a_\gamma, b_\gamma, c_\gamma) = (4.752, -3.318, 0.59), \\ Nu = \gamma F_S. \end{cases}$$ (2.12)

The general form of the proposed parametrization was suggested by heuristic arguments in Radko (2008) and Radko & Smith (2012). Since the parametrization (2.12) was derived using simulations for relatively low density ratios, it is not expected to capture the non-monotonic character of the flux ratio (figure 1), for which the minimum occurs at $R_{\rho\,min} \sim 4$ (Schmitt 1979a). The flux pattern for $\bar{\bar{R}}_\rho > 2$ is of secondary importance since, in this regime, finger-induced transport in the ocean is weak and has very limited impact on the large-scale dynamics.

The flux-gradient model assumes that mixing dependences deduced from linear-gradient simulations are also applicable to the local fine-scale conditions in inhomogeneous stratification and can be used to parametrize $Nu(\bar{R}_\rho)$ and $\gamma(\bar{R}_\rho)$. Therefore, A_{Nu} and A_γ were evaluated using (2.12). The positive root of (2.4) for $\bar{\bar{R}}_\rho = 1.5$ is

$$\lambda_{norm} = \frac{\lambda}{m^2} = 6.348.$$ (2.13)

For the experiment in figure 5 ($m = 2\pi/H = 0.0157$, $\bar{\bar{R}}_\rho = 1.5$), the expression (2.13) translates to $\lambda_{theor} = 1.565 \times 10^{-3}$, which agrees with the numerically inferred growth rate (2.11) to within 6 %.

The success of the flux-gradient theory in predicting the growth rate for the experiment in figure 5 is not surprising. The vertical scale of the amplifying mode is relatively large ($H = 400$) and therefore clear scale separation exists between this mode and the scale of individual fingers ($d \sim 10$). The question that arises at this point is whether similar agreement can be expected for smaller values of H. To address this concern, a series of eight simulations has been performed in which the height of the computational domain was set to $H = 50, 100, 150, \ldots, 400$. In other respects, these simulations were analogous to the DNS in figure 5. For each experiment, the initial perturbation was represented by the fundamental harmonic. The growth rate λ_{num} was calculated from the exponential fit (2.10) of the time record of its amplitude $A_T(t)$ during the period of linear growth. The numerical growth rates are plotted in figure 6(a,b) along with the theoretical prediction $\lambda_{theor} = \lambda_{norm}(2\pi/H)^2$, where
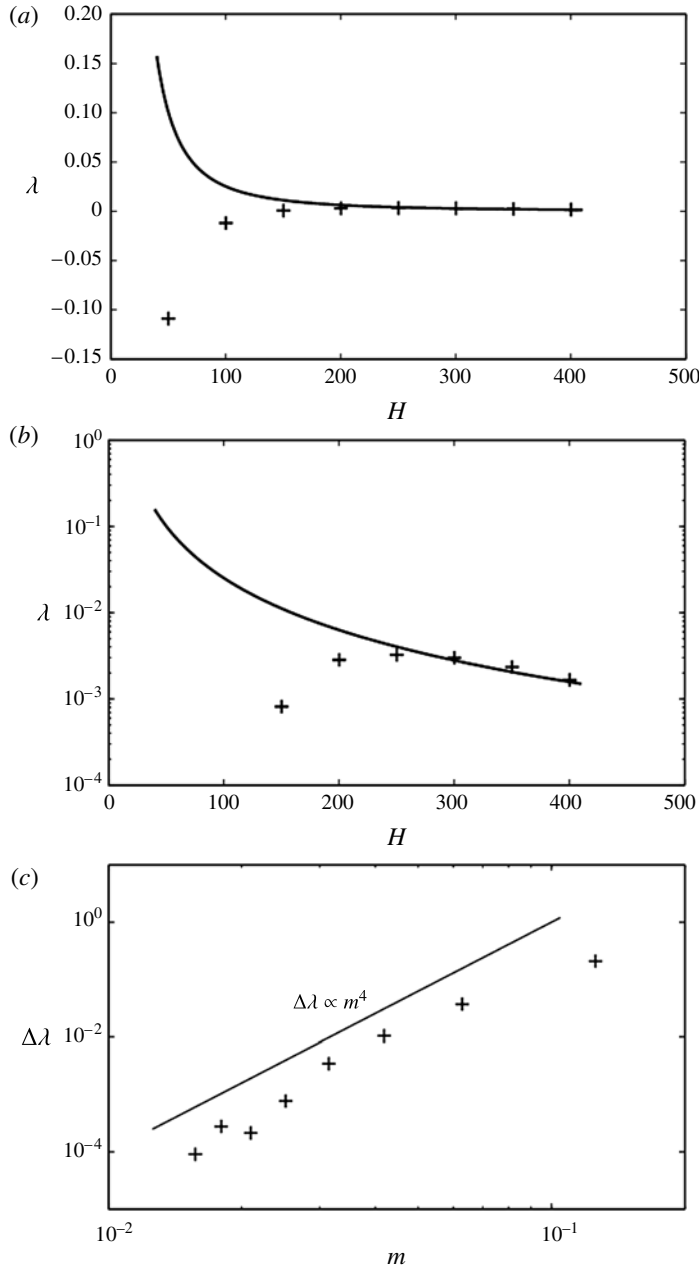
FIGURE 6. (*a*) The growth rates of layering modes diagnosed from DNS (indicated by plus signs) are plotted as a function of the perturbation wavelength along with the theoretical prediction based on the flux-gradient theory. (*b*) The same as in (*a*) but the growth rate is plotted on the logarithmic scale (only the positive growth rates are shown). The flux-gradient theory is fully consistent with DNS for large wavelengths ($H \geqslant 250$) but fails for small ones ($H < 250$). (*c*) The difference in the growth rates predicted by the flux-gradient model and diagnosed from DNS is plotted as a function of wavenumber $m = 2\pi/H$ in logarithmic coordinates, along with the straight line with the slope corresponding to a power law $\Delta\lambda \propto m^4$.

λ_{norm} is given by (2.13). The results are suggestive: for $H \geqslant 250$, the flux-gradient theory is successful in predicting the numerical growth rates, but its performance dramatically deteriorates for $H \leqslant 200$. For $H \leqslant 150$, the flux-gradient theory even fails to correctly predict the sign of the growth rate. Figure 6(c) plots the deviation of the theoretical prediction from the numerical results, $\Delta\lambda = |\lambda_{num} - \lambda_{theor}|$, as a function of the wavenumber m in logarithmic coordinates. The data points in figure 6(c) tend to align along the straight line corresponding to $\Delta\lambda \propto m^4$. This specific pattern in the error growth with increasing wavenumbers is significant and will guide the modification of flux-gradient models aimed at correcting their unphysical behaviour at small scales (§ 6).

The instances of the applicability or failure of the flux-gradient model are remarkably consistent across the full range of parameters $(\bar{\bar{R}}_\rho, H)$ considered in this study. The scale separation between fingers and gamma-instability modes by approximately a factor of 20 appears to constitute both a necessary and sufficient condition for the adequate performance of the model. However, the mechanisms responsible for the failure of the flux-gradient laws at small scales are poorly understood, and a predictive analytical theory for the point-of-failure scale H_{pof} is missing. The flux-gradient laws themselves are internally consistent and provide no guidance with regard to their range of validity. Therefore, we turn to an alternative framework for the analysis of layering instability based on the techniques of multiscale analysis. The multiscale model holds the promise of conceptualizing the point-of-failure effect due to its explicit treatment of the interactions between fingers and larger layering modes.

3. Layering instability as a multiscale problem

In addition to the flux-gradient model reviewed in § 2, spontaneous layering in salt-finger favourable stratification can be described using multiscale methods. Our layering model is analogous to the multiscale models of collective instability (Holyer 1981, 1985) and thermohaline interleaving (Radko 2011). It also bears resemblance to the multiscale analyses of mixing in one-component flows (Balmforth & Young 2002, 2005) and to models illustrating spontaneous generation of planetary-scale flows by mesoscale variability (Manfroi & Young 1999, 2002). The starting point for such analyses is the choice of the periodic small-scale pattern, which is frequently represented by the Kolmogorov solution – the steady sinusoidal background flow. The steady state is maintained by introducing into the governing equations a synthetic external forcing term, conforming to the chosen background pattern (Meshalkin & Sinai 1961; Sivashinsky 1985).

In this study, we also use the Kolmogorov-based approach. For simplicity, we consider the 2D flow, although the extension to three dimensions is fairly straightforward. The governing equations (2.1) are augmented by adding the forcing function and written in 2D form as follows:

$$\begin{cases} \dfrac{\partial T}{\partial t} + J(\psi, T) + \dfrac{\partial \psi}{\partial x} = \nabla^2 T + f_T, \\[2mm] \dfrac{\partial S}{\partial t} + J(\psi, S) + \dfrac{1}{\bar{\bar{R}}_\rho} \dfrac{\partial \psi}{\partial x} = \tau \nabla^2 S + f_S, \\[2mm] \dfrac{\partial}{\partial t} \nabla^2 \psi + J(\psi, \nabla^2 \psi) = Pr \left[\dfrac{\partial}{\partial x}(T - S) + \nabla^4 \psi \right] + f_M, \end{cases} \quad (3.1)$$

where ψ is the streamfunction, $J(a, b) = (\partial a/\partial x)(\partial b/\partial z) - (\partial a/\partial z)(\partial b/\partial x)$ is the Jacobian, and (f_T, f_S, f_M) is the forcing term. The basic state is taken in the form of vertical salt fingers, so-called elevator modes:

$$\begin{cases} T_{bg} = \hat{T}_{bg} \sin(kx), \\ S_{bg} = \hat{S}_{bg} \sin(kx), \\ \psi_{bg} = \hat{\psi}_{bg} \cos(kx), \end{cases} \tag{3.2}$$

where k corresponds to the fastest-growing finger mode in the unforced system (k_{max}). The fastest-growing wavelength clearly dominates the pattern of fully developed fingers (Gargett & Schmitt 1982; Stern *et al.* 2001; Traxler *et al.* 2011). Therefore, solutions based on the fastest-growing mode offer a much more realistic and physical representation of salt fingering than, for instance, the elevator mode with zero growth rate ($k = k_0$). The latter truly steady solution has also been used as a background pattern for earlier multiscale expansions (e.g. Holyer 1981, 1985). However, for the layering problem considered herein, the advantages of focusing a multiscale analysis on the fastest-growing mode ($k = k_{max}$) are critical. The arguments presented in Radko (2003), and reviewed in § 2, suggest that double-diffusive layering is highly sensitive to the variation in the flux ratio with the density ratio. The fastest-growing finger model (Schmitt 1979*a*) is able to capture the flux ratio pattern realized in numerical (e.g. Radko & Smith 2012) and laboratory (e.g. Schmitt 1979*b*) experiments with surprising accuracy. On the other hand, the model based on the elevator mode with zero growth rate completely misrepresents the flux ratio pattern, which precludes its use in multiscale analyses of layering.

Another notable feature of the presented model is related to the microscale instability of our background pattern. Most multiscale models assume stable background patterns (e.g. Gama, Vergassola & Frisch 1994; Novikov & Papanicolau 2001; Legras & Villone 2009). In such cases, the maintenance of a steady state amounts to the prevention of its gradual dissipation, which is readily accomplished by adding the corresponding forcing function to the governing equations. In our case, the background pattern is unstable, and therefore the forcing function is introduced to arrest its growth. The physical interpretations of these two types of forced systems, stable and unstable, are also subtly different. In the former case, the forcing represents the ultimate source of small-scale variability that may be difficult or otherwise undesirable to incorporate in the model formulation. In the present model, the source of variability – the primary salt-finger instability – is introduced explicitly and the forcing function represents processes that are involved only in the equilibration of its linear growth.

The equilibration dynamics of salt fingers was most recently considered by Radko & Smith (2012), who attributed the saturation of primary fastest-growing modes to the nonlinear adverse action of their secondary microscale instabilities. Importantly, even after its equilibration, the fastest-growing mode continues to dominate the microscale *T*–*S* patterns. The fact that this mode remains statistically steady implies that, on average, its linear growth is balanced by the corresponding $k = k_{max}$ components of the nonlinear tendency terms in the governing equations. Furthermore, since the fastest-growing mode dominates the equilibrium (T, S, ψ) distribution, the balancing nonlinear terms should also be dominated by the same harmonic ($k = k_{max}$). In the present multiscale model, these nonlinear equilibrating processes are represented by forcing functions (f_T, f_S, f_M).

The explicit expression for the equilibrating forcing function is obtained by requiring the background pattern (3.2) to be steady, which results in

$$
\begin{cases}
f_T = [k^2 \hat{T}_{bg} - k \hat{\psi}_{bg}] \sin(kx), \\
f_S = \left[\tau k^2 \hat{S}_{bg} - \dfrac{k}{\bar{\bar{R}}_\rho} \hat{\psi}_{bg} \right] \sin(kx), \\
f_M = [k(\hat{S}_{bg} - \hat{T}_{bg}) - k^4 \hat{\psi}_{bg}] \cos(kx).
\end{cases}
\tag{3.3}
$$

We are interested in the asymptotic stability of the basic state (3.2) with respect to slow, horizontally uniform, long-wavelength perturbations. This is accomplished by separating the dependent variables into the steady background field of salt fingers $(T_{bg}, S_{bg}, \psi_{bg})$ and a weak perturbation (T', S', ψ'). Linearization of the governing set (3.1) about the basic state yields:

$$
\begin{cases}
\dfrac{\partial T'}{\partial t} - \hat{\psi}_{bg} k \sin(kx) \dfrac{\partial T'}{\partial z} - \hat{T}_{bg} k \cos(kx) \dfrac{\partial \psi'}{\partial z} + \dfrac{\partial \psi'}{\partial x} = \nabla^2 T', \\
\dfrac{\partial S'}{\partial t} - \hat{\psi}_{bg} k \sin(kx) \dfrac{\partial S'}{\partial z} - \hat{S}_{bg} k \cos(kx) \dfrac{\partial \psi'}{\partial z} + \dfrac{1}{\bar{\bar{R}}_\rho} \dfrac{\partial \psi'}{\partial x} = \tau \nabla^2 S', \\
\dfrac{\partial}{\partial t} \nabla^2 \psi' - \hat{\psi}_{bg} k \sin(kx) \dfrac{\partial}{\partial z} \nabla^2 \psi' - \hat{\psi}_{bg} k^3 \sin(kx) \dfrac{\partial \psi'}{\partial z} = Pr \left[\dfrac{\partial}{\partial x}(T' - S') + \nabla^4 \psi' \right].
\end{cases}
\tag{3.4}
$$

Next, new spatial and temporal variables (Z, t_0) are introduced, which are related to the original variables as follows:

$$
Z = \varepsilon z, \quad t_0 = \varepsilon^2 t,
\tag{3.5a,b}
$$

where $\varepsilon = d/L$ is the expansion parameter representing the difference in spatial scales of primary (fingering) and secondary (layering) instabilities – d and L, respectively. On short spatial scales, we impose the same periodicity as in the basic flow and derivatives in the linearized system (3.4) are replaced as follows:

$$
\frac{\partial}{\partial t} \rightarrow \varepsilon^2 \frac{\partial}{\partial t_0}, \quad \frac{\partial}{\partial z} \rightarrow \varepsilon \frac{\partial}{\partial Z}.
\tag{3.6a,b}
$$

To examine the interaction of the homogeneous salt-finger field with large scales in the asymptotic limit $\varepsilon \ll 1$, we search for solutions in terms of a series in ε:

$$
(T', S', \psi') = (T_0, S_0, \psi_0) + \varepsilon(T_1, S_1, \psi_1) + \varepsilon^2(T_2, S_2, \psi_2) + \cdots.
\tag{3.7}
$$

Equations (3.6) and (3.7) are substituted in (3.4), terms of the same order in ε are collected, and the resulting hierarchy of equations is sequentially solved until a closed explicit solution is found as detailed below.

Our focus is on the evolution of large-scale flows, and therefore it is natural to open the expansion with the long-wavelength horizontally uniform perturbations in temperature and salinity. The zero-order balances of the governing equations demand that there be no additional terms with variation on the short spatial scale in (T_0, S_0) and therefore

$$
\begin{cases}
T_0 = T_0(Z, t_0), \\
S_0 = S_0(Z, t_0).
\end{cases}
\tag{3.8}
$$

The interaction of the large-scale modes with the basic field results in the appearance of T–S modes proportional to $\sin(kx)$, but modulated vertically at long scales, and of the associated streamfunction modes proportional to $\cos(kx)$. Thus, the first-order solution is sought in the following form:

$$\begin{cases} T_1 = T_{1B}(Z, t_0) \sin(kx), \\ S_1 = S_{1B}(Z, t_0) \sin(kx), \\ \psi_1 = \psi_{1A}(Z, t_0) \cos(kx). \end{cases} \tag{3.9}$$

Substituting (3.9) in the first-order balance of (3.4) makes it possible to express the first-order components in terms of zero-order quantities:

$$\begin{cases} T_{1B} = \dfrac{\hat{\psi}_{bg}\left((k^4\tau\bar{\bar{R}}_\rho - 1)\dfrac{\partial T_0}{\partial Z} + \bar{\bar{R}}_\rho\dfrac{\partial S_0}{\partial Z}\right)}{k(\tau k^4\bar{\bar{R}}_\rho + \tau\bar{\bar{R}}_\rho - 1)}, \\[4mm] S_{1B} = \dfrac{\hat{\psi}_{bg}\left(-\dfrac{\partial T_0}{\partial Z} + \dfrac{\partial S_0}{\partial Z}\bar{\bar{R}}_\rho(1 + k^4)\right)}{k(\tau k^4\bar{\bar{R}}_\rho + \tau\bar{\bar{R}}_\rho - 1)}, \\[4mm] \psi_{1A} = \dfrac{\hat{\psi}_{bg}\left(\dfrac{\partial S_0}{\partial Z} - \tau\dfrac{\partial T_0}{\partial Z}\right)\bar{\bar{R}}_\rho}{\tau k^4\bar{\bar{R}}_\rho + \tau\bar{\bar{R}}_\rho - 1}. \end{cases} \tag{3.10}$$

The solution sought is obtained at the second order. When the $O(\varepsilon^2)$ components of system (3.4) are averaged in x and (3.10) is used to simplify the result, we arrive at

$$\begin{cases} \dfrac{\partial T_0}{\partial t_0} = a_T\dfrac{\partial^2 T_0}{\partial Z^2} + b_T\dfrac{\partial^2 S_0}{\partial Z^2}, \\[4mm] \dfrac{\partial S_0}{\partial t_0} = a_S\dfrac{\partial^2 T_0}{\partial Z^2} + b_S\dfrac{\partial^2 S_0}{\partial Z^2}, \end{cases} \tag{3.11}$$

where

$$\begin{cases} a_T = 1 - \dfrac{\hat{\psi}_{bg}^2(1 - \tau k^4\bar{\bar{R}}_\rho) + \hat{T}_{bg}\hat{\psi}_{bg}k\tau\bar{\bar{R}}_\rho}{2(\tau k^4\bar{\bar{R}}_\rho + \tau\bar{\bar{R}}_\rho - 1)}, \quad b_T = \dfrac{\hat{\psi}_{bg}^2\bar{\bar{R}}_\rho + k\hat{\psi}_{bg}\hat{T}_{bg}}{2(\tau k^4\bar{\bar{R}}_\rho + \tau\bar{\bar{R}}_\rho - 1)}, \\[4mm] a_S = -\dfrac{\hat{\psi}_{bg}^2 + \tau k\hat{\psi}_{bg}\hat{S}_{bg}\bar{\bar{R}}_\rho}{2(\tau k^4\bar{\bar{R}}_\rho + \tau\bar{\bar{R}}_\rho - 1)}, \quad b_S = \tau + \dfrac{k\hat{\psi}_{bg}\hat{S}_{bg}\bar{\bar{R}}_\rho + \hat{\psi}_{bg}^2\bar{\bar{R}}_\rho(1 + k^4)}{2(\tau k^4\bar{\bar{R}}_\rho + \tau\bar{\bar{R}}_\rho - 1)}. \end{cases} \tag{3.12}$$

System (3.11) represents a closed set of equations written entirely in terms of rescaled spatial and temporal variables (Z, t_0). At this point, the multiscale analysis is complete and we can safely return to the original variables (z, t) by inverting transformation (3.5). The stability of the resulting system is analysed using normal modes,

$$(T_0, S_0) = (\hat{T}_0, \hat{S}_0)\exp(\lambda_{ms}t)\sin(mz), \tag{3.13}$$

which produce the growth-rate equation

$$\lambda_{ms,norm}^2 + \lambda_{ms,norm}(a_T + b_S) + (a_Tb_S - a_Sb_T) = 0, \tag{3.14}$$

where $\lambda_{ms,norm} = \lambda_{ms} m^{-2}$ is the normalized growth rate. According to (3.12) and (3.14), $\lambda_{ms,norm}$ is determined by the background pattern and is independent of m. Therefore, the dependence of the growth rate on the vertical wavenumber takes a simple quadratic form

$$\lambda_{ms} = \lambda_{ms,norm} m^2. \tag{3.15}$$

The growth-rate equation (3.14) suggested by the multiscale theory is structurally analogous to its flux-gradient counterpart (2.4). The connection between the two models, however, is not limited to their formal similarity. For instance, it is of interest to examine the link between λ_{ms} and the flux ratio pattern in the growing layering modes (appendix A), which takes the form

$$\lambda_{ms} = \frac{\partial \gamma}{\partial \bar{\bar{R}}_\rho} \frac{\bar{\bar{R}}_\rho (\hat{w}_{bg} \hat{S}_{bg} - 2\tau \bar{\bar{R}}_\rho)(\hat{T}_0 - \bar{\bar{R}}_\rho \hat{S}_0)}{2(\hat{T}_0 - \gamma_{bg} \hat{S}_0)} m^2, \tag{3.16}$$

where $\hat{w}_{bg}$ is the amplitude of the vertical velocity in the background state (3.2), $\gamma_{bg} = \hat{T}_{bg}/\hat{S}_{bg}$ is its flux ratio and $\partial \gamma / \partial \bar{\bar{R}}_\rho$ is the variation of the flux ratio with the density ratio in the linear normal mode (3.13). Equation (3.16) indicates that perturbation growth in the multiscale model is possible only if the flux ratio varies with the density ratio. Furthermore, extensive experimentation with the multiscale model indicates that the coefficient of $\partial \gamma / \partial \bar{\bar{R}}_\rho$ is negative for background patterns that offer a qualitatively consistent representation of salt fingers $(0 < \hat{T}_{bg}/\hat{S}_{bg} < 1, \ (\hat{T}_{bg}, \hat{S}_{bg}, \hat{w}_{bg}) = O(10), \ \hat{T}_{bg}/\hat{w}_{bg} < 0)$. Thus, layering instability of a finger-favourable gradient in both models, flux-gradient and multiscale, is driven by the gamma-effect – a decrease in the flux ratio with the density ratio.

Despite the direct connection between the flux-gradient and multiscale models, their strengths and limitations differ considerably. The roles that these models play in the theory of double diffusion are complementary. For instance, a clear advantage of the multiscale model lies in its explicit representation of microscale dynamics, which makes it possible to identify the point of breakdown of multiscale solutions at finite values of $\varepsilon = d/L$. In contrast, the flux-gradient model by itself offers no clues with regard to its range of validity. Therefore, in the next section we shall compare the asymptotic ($\varepsilon \to 0$) multiscale model with its finite-amplitude counterpart to explain the mechanisms of the point-of-failure effect.

4. Failure of the multiscale expansion

The essence of the multiscale model (§ 3) is the stability analysis of the background fingering state (3.2) in the asymptotic limit $\varepsilon \to 0$. A natural way to determine the accuracy of this expansion is through a comparison of the asymptotic solutions with their finite-ε counterparts. For finite ε, the linear stability of the spatially periodic system (3.2) has been analysed using two methods. We have considered a Floquet-based technique in which normal modes are assumed to be harmonic in z and represented in terms of Fourier series in x – see Holyer (1984) or Radko & Smith (2012), where this method was applied to the salt-finger problem. The second approach is based on the Fourier-truncated Galerkin projection of the following form:

$$\begin{cases} T' = [\tilde{T}_0 + \tilde{T}_1 \sin(kx)] \exp(\lambda t + imz), \\ S' = [\tilde{S}_0 + \tilde{S}_1 \sin(kx)] \exp(\lambda t + imz), \\ \psi' = \tilde{\psi}_1 \cos(kx) \exp(\lambda t + imz). \end{cases} \tag{4.1}$$

The Floquet-based and truncated solutions were found to be mutually consistent, and therefore the following discussion is based on the much simpler truncated model (4.1). One can easily recognize that the truncated system represents the immediate generalization of the asymptotic ($\varepsilon \to 0$) solutions in §3. The key difference is that the truncated model makes no assumption with regard to the magnitude of ε. Hence, the deviation of the truncated solutions based on (4.1) from their asymptotic counterparts (§3) can be used to evaluate the error of the multiscale model and to identify its range of validity.

The eigenvalue equation for the truncated model is derived as follows: (i) the truncated system (4.1) is substituted in the linearized equations (3.4), (ii) the projections of the resulting equations onto the Fourier modes used in (4.1) are determined, and (iii) the modal amplitudes ($\tilde{T}_0, \tilde{T}_1, \tilde{S}_0, \tilde{S}_1, \tilde{\psi}_1$) are sequentially eliminated. The result is the growth-rate equation that takes the form of the fifth-degree polynomial

$$\sum_{n=0}^{5} a_n \lambda^n = 0, \qquad (4.2)$$

whose coefficients are represented by algebraic expressions in terms of

$$a_n = a_n(m, k, \hat{T}_{bg}, \hat{S}_{bg}, \hat{\psi}_{bg}, \bar{\bar{R}}_\rho, \tau). \qquad (4.3)$$

The solutions of the truncated model obtained for various parameters are structurally similar to each other. A typical calculation is shown in figure 7, which presents the solution of the growth-rate equation (4.2) as a function of vertical wavenumber m (solid curves) along with the corresponding estimate of the growth rate based on the multiscale model (3.14) indicated by the dashed curve. As expected, the multiscale and truncated models agree closely for low values of m but diverge as m increases. The pattern of the $\lambda(m)$ relation predicted by the truncated model in the $\text{Re}(\lambda) > 0$ region is characterized by two approximately symmetric branches, which coalesce at the bifurcation point (m_b, λ_b). Prior to coalescence $(m < m_b)$, both branches are purely real, and after coalescence $(m > m_b)$, the growth rate attains large imaginary component. The lower branch (indicated by the heavy curve) represents the layering modes, dominated by horizontally uniform harmonics $(T', S') \propto \exp(imz)$ – the modes captured by the asymptotic analysis in §3. The modes represented by the upper branch (light curve) and its large-wavenumber extension $(m > m_b)$ have a considerably different spatial structure. They are controlled by Fourier harmonics with finite horizontal width $(T', S') \propto \sin(kx) \exp(imz)$, and therefore these modes *per se* are of limited interest in our investigation. However, analysis of the upper branch has led us to useful inferences about the dynamics of layering modes as follows. The maximum growth rate on the upper branch can be estimated by considering the limit $m \to 0$, $\tau \to 0$ of the growth-rate equation, which results in

$$\lambda_{max} \approx \frac{4Pr}{k^2 \bar{\bar{R}}_\rho (1 + Pr)^2}. \qquad (4.4)$$

Given the approximate symmetry of the two branches in figure 7, we estimate the growth rate at the bifurcation point $\lambda_b \approx \lambda_{max}/2$. Furthermore, noting that at the bifurcation point (m_b) the asymptotic growth rate λ_{ms} underestimates the value suggested by the truncated model (λ_b) by approximately a factor of 2, we assume

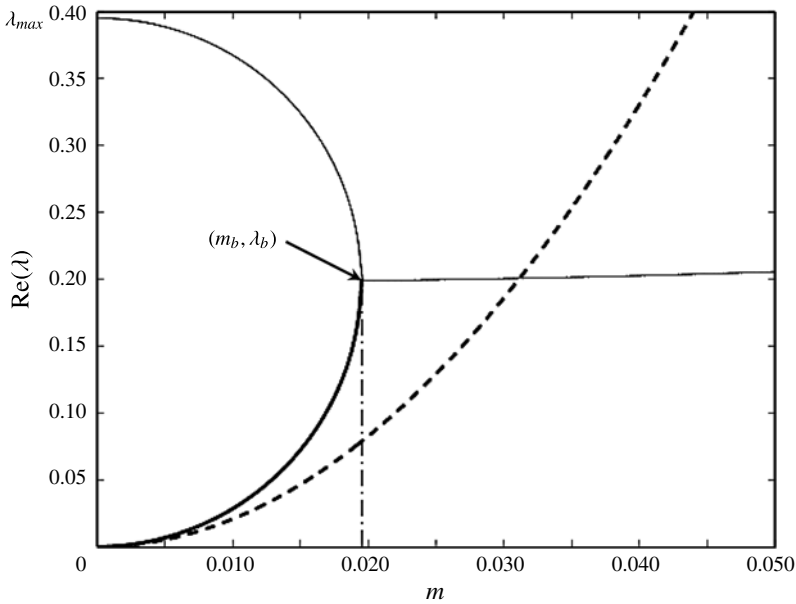$$\lambda_{ms,norm} m_b^2 \sim \frac{\lambda_b}{2} \sim \frac{Pr}{k^2 \bar{\bar{R}}_\rho (1 + Pr)^2}. \qquad (4.5)$$

FIGURE 7. A typical stability diagram for the basic state consisting of vertical 2D fingers (3.2). This calculation is made for $(\bar{\bar{R}}_\rho, Pr, \tau) = (1.5, 7, 0.01)$, the wavelength of the most unstable mode is $k = 0.8$ and the amplitude of the background pattern $(\hat{T}_{bg}, \hat{S}_{bg}, \hat{\psi}_{bg}) = (3.91, 6.52, 4.77)$ is inferred from the corresponding DNS. The dashed curve represents the multiscale model, which assumes a significant scale separation between fingers and layering modes. The solid curve represents a generalization of the stability analysis that does not rely on scale separation; its portion corresponding to layering modes is indicated by larger line width. The multiscale and generalized solutions are consistent for low wavenumbers but diverge for large ones. No unstable layering solutions are found using the generalized model for $m > m_b$.

Finally, we note that the asymptotic and truncated models are qualitatively consistent (within a factor of 2) over the interval $0 < m < m_b$ but become completely different outside of it. Based on this assumption, we predict the wavelength (H_{pof}) for the point of failure of the asymptotic expansion using (4.5) as follows:

$$H_{pof} \sim \frac{2\pi}{m_b} \sim 2\pi k(1 + Pr)\sqrt{\bar{\bar{R}}_\rho \lambda_{ms,norm}/Pr}. \tag{4.6}$$

The analysis offered in this section leads to a plausible physical explanation for the failure of the flux-gradient model at small scales and its dramatic manifestation in terms of the ultraviolet catastrophe. We have argued that vertically elongated salt fingers are linearly stable with respect to relatively short, horizontally uniform, perturbations and therefore modes with $H < H_{pof}$ are damped. Since the microscale dynamics at such a detailed level are not represented by the flux-gradient model, it is not surprising that it does not describe the short-wave stabilization effect. Likewise, the multiscale model (§ 3), which, from the outset, assumes an asymptotically large scale separation between layering modes and fingers, becomes equally unreliable on finger scales. The DNS presented in § 2, on the other hand, are free from the limitations of flux-gradient and multiscale models and therefore they reveal the

short-wave stabilization very clearly (figures 4 and 6). Next, we proceed to estimate typical values of the point-of-failure scale suggested by (4.6) and compare it with that observed in DNS.

5. Validation of the point-of-failure theory

The prediction of the point-of-failure scale (4.6) is the key result of the analytical theory. The combination of (3.14) and (4.6) makes it possible to evaluate H_{pof} for any given amplitude of the background pattern $(\hat{T}_{bg}, \hat{S}_{bg}, \hat{\psi}_{bg})$. However, in terms of practical implementations, it is desirable to express H_{pof} in terms of more widely used quantities that are directly accessible from field measurements, laboratory experiments or simulations. For instance, it is straightforward to base our estimates on the salt flux F_S maintained by the basic state (3.2):

$$F_S = \hat{S}_{bg}\hat{w}_{bg}\overline{\sin^2 kx} = \tfrac{1}{2}\hat{S}_{bg}\hat{\psi}_{bg}k. \qquad (5.1)$$

Based on the existing observational and numerical evidence (e.g. Gargett & Schmitt 1982; Shen & Schmitt 1995), we assume that the representative wavenumber k and the amplitude ratios $(\gamma_{bg} = \hat{T}_{bg}/\hat{S}_{bg}$ and $\gamma_{bg,\psi} = \hat{\psi}_{bg}/\hat{S}_{bg})$ are adequately predicted by the fastest-growing finger model (Schmitt 1979a). Therefore, the finger amplitude vector $(\hat{T}_{bg}, \hat{S}_{bg}, \hat{\psi}_{bg})$ is linked to F_S through

$$\hat{S}_{bg} \sim \sqrt{\frac{2F_S}{k\gamma_{bg,\psi}}}, \quad \hat{T}_{bg} \sim \gamma_{bg}\sqrt{\frac{2F_S}{k\gamma_{bg,\psi}}}, \quad \hat{\psi}_{bg} \sim \sqrt{\frac{2F_S\gamma_{bg,\psi}}{k}}. \qquad (5.2a\text{--}c)$$

The salt flux can be deduced from various sources: laboratory experiments (e.g. Schmitt 1979b), oceanographic field measurements (e.g. Schmitt *et al.* 2005; Bryden *et al.* 2014), numerical simulations (e.g. Traxler *et al.* 2011) or even other analytical models designed specifically to predict the equilibrium transport (e.g. Radko 2008; Radko & Smith 2012).

For instance, an estimate of H_{pof} can be based on oceanographic measurements of mixing in thermohaline staircases. In high-gradient interfaces of well-defined staircases, double diffusion is apparently the dominant mixing process, which removes any ambiguity in the interpretation of mixing data. However, since the analytical model (§§ 3 and 4) assumes an effectively unbounded domain, a question can be raised whether the local T–S diffusivities measured in relatively thin interfaces are suitable for our purpose. While the convecting layers in staircases undoubtedly influence the dynamics of interfaces, observations (e.g. Bryden *et al.* 2014) suggest that the local diffusivities in interfaces are comparable to their smooth-gradient counterparts. This proposition will also be supported and quantified by the numerical models of staircases in § 6.

Reliable estimates of vertical transport are now available for the two major salt-finger staircases, located in the Caribbean Sea (Schmitt *et al.* 2005) and in the western Mediterranean (Bryden *et al.* 2014). Table 1 summarizes their typical geometric characteristics, along with the corresponding estimates of the vertical salt flux. The salt flux for the Caribbean staircase was obtained from the tracer release experiment, and the western Mediterranean flux was inferred from the analysis of the large-scale salinity budget. These fluxes were non-dimensionalized using the T–S gradients in salt-finger interfaces as the basic state $(\bar{\bar{T}}_{z,dim}, \bar{\bar{S}}_{z,dim})$, resulting in $F_S = 97$

	Western Mediterranean	Caribbean
Interfacial salinity gradient (p.s.u. m^{-1})	1.2×10^{-3}	0.05
Interfacial temperature gradient (°C m^{-1})	5.1×10^{-3}	0.3
Overall salinity gradient (p.s.u. m^{-1})	0.95×10^{-4}	0.005
Overall temperature gradient (°C m^{-1})	4.1×10^{-4}	0.03
Interface height (m)	6	2
Layer height (m)	75	20
$F_{S,dim}$ (p.s.u. m s^{-1})	5.3×10^{-8}	4.3×10^{-7}
F_S	196	97
R_ρ	1.3	1.6
H_{pof}	347	331

TABLE 1. Representative characteristics of two thermohaline staircases located in the Caribbean and in the western Mediterranean. Based on the data in Kunze (2003), Schmitt *et al.* (2005) and Bryden *et al.* (2014).

and $F_S = 196$ for the Caribbean and the western Mediterranean conditions, respectively. Next, the point-of-failure scale was estimated using (3.14), (4.6) and (5.2), yielding $H_{pof} = 331$ for the Caribbean and $H_{pof} = 347$ for the western Mediterranean. These estimates are generally consistent with the point-of-failure scales deduced from the DNS (figure 6). The observationally inferred values are slightly higher, but not more than by a factor of 2. This is an encouraging result, given that both observational estimates of fluxes and the theoretical model leading to (4.6) involve significant approximations. Also suggestive is the finding that these calculations, obtained for very dissimilar staircases, yield comparable values of H_{pof}. This can be interpreted as evidence for the robust nature of the point-of-failure scale and its limited sensitivity to environmental conditions.

Of course, the alternative – and the most convenient – way of estimating H_{pof} is to use the numerically derived values of F_S, which are available for a wide range of density ratios by virtue of (2.12). The observational and numerical estimates of the point-of-failure scale (4.6) are plotted in figure 8(a) as a function of $\bar{\bar{R}}_\rho$, which shows that these two approaches are mutually consistent. The typical point-of-failure scale deduced from observations is only slightly larger than its numerical counterpart (figure 8a), and they both reveal the pronounced lack of variability in $H_{pof}(\bar{\bar{R}}_\rho)$. As the density ratio varies from 1.1 to 1.8, which covers all known instances of finger-induced layering in the ocean, the point-of-failure scale changes by $\sim 15\%$.

To be more systematic in assessing the accuracy of the predictions in figure 8(a), we have performed a series of 48 DNS analogous to those in figures 5 and 6, with various density ratios ($\bar{\bar{R}}_\rho = 1.2, 1.3, \ldots, 1.7$) and wavelengths ($H = 50, 100, \ldots, 400$). Each simulation was initiated with the small-amplitude fundamental harmonic (2.9). Its growth rate was diagnosed from simulations (λ_{num}) and then compared with the corresponding growth rate (λ_{theor}) suggested by the flux-gradient model (2.4). The ratio $\lambda_{num}/\lambda_{theor}$ is plotted as a function of $\bar{\bar{R}}_\rho$ and H in figure 8(b). Despite some scatter in the numerical data, it is clear that these results are generally consistent with the point-of-failure theory (figure 8a). For relatively large scales ($H > 300$), the growth rate is well represented (with the error less than 10 %) by the flux-gradient model. The reduction in H to 200–250 leads to the rapid deterioration in the predictive capabilities of the flux-gradient model. For $H < 150$, the numerical solutions (in contrast with their
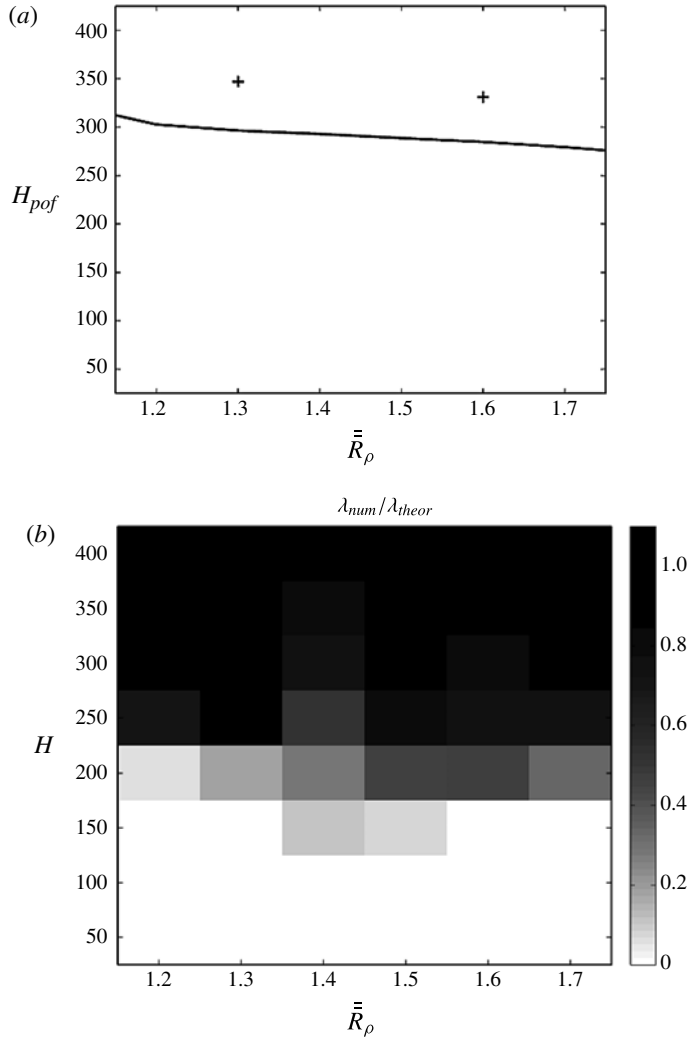
FIGURE 8. (*a*) The point-of-failure scale H_{pof} suggested by theoretical arguments is plotted as a function of the background density ratio. The calculations indicated by solid curve (plus signs) use numerically (observationally) derived fluxes. (*b*) The quality assessment of the flux-gradient laws. The ratio of the layering growth rates diagnosed from DNS and evaluated using the flux-gradient theory are plotted as a function of the density ratio and the vertical wavelength. Only positive values are shown. Both theory (*a*) and DNS (*b*) indicate that the flux laws are reasonably accurate for $H \geqslant 250$ but fail for $H < 250$ regardless of the density ratio.

flux-gradient counterparts) are characterized by the decay of perturbations. Another prominent feature of the diagnostics in figure 8(*b*), which is also consistent with the point-of-failure theory, is the lack of systematic variation in $\lambda_{num}/\lambda_{theor}$ with $\bar{\bar{R}}_\rho$. For all density ratios considered, $H \sim 200$–300 appears to represent the universal threshold for the validity of the flux-gradient model.

The systematic failure of the flux-gradient laws at small scales raises the question of whether they can be altered in a way that would capture the observed (figures 6

and 8*b*) stabilization of high wavenumbers. In the following section, we consider a simple model of this nature.

6. Flux-gradient-aberrancy laws

6.1. *Formulation and calibration*

An obvious candidate for selective damping of high wavenumbers is biharmonic diffusion. As suggested by Radko (2005) the flux-gradient model (2.3) can be modified as follows:

$$\begin{cases} \dfrac{\partial \bar{T}}{\partial t} = -\dfrac{\partial}{\partial z} F_T = \dfrac{\partial}{\partial z}\left(Nu\dfrac{\partial \bar{T}}{\partial z}\right) - \mu \dfrac{\partial^4 \bar{T}}{\partial z^4}, \\[3mm] \dfrac{\partial \bar{S}}{\partial t} = -\dfrac{\partial}{\partial z} F_S = \dfrac{\partial}{\partial z}\left(\dfrac{Nu}{\gamma}\dfrac{\partial \bar{T}}{\partial z}\right) - \mu \dfrac{\partial^4 \bar{S}}{\partial z^4}, \end{cases} \tag{6.1}$$

where the biharmonic coefficient μ depends on the background density ratio. Relatively large scales are mostly unaffected by the inclusion of biharmonic terms, but small ones rapidly decay. The inclusion of the fourth-order derivatives in the model formulation is consistent with the observation (figure 6*c*) that the error of the flux-gradient model in predicting the layering growth rate increases with the wavenumber as $\propto m^4$. The expressions for vertical fluxes (F_T, F_S) in the model (6.1) now include components of two types: those determined by the first derivatives of $\bar{T}$ and $\bar{S}$ (gradient terms) and by their third derivatives (aberrancy terms). Therefore, this formulation will be referred to hereafter as the flux-gradient-aberrancy laws.

Some justification for introducing flux laws in this form can be derived from the following argument. First, we note that in the most general form, we expect double-diffusive fluxes at any location z_0 to be controlled by the large-scale T–S patterns in its immediate vicinity. This pattern can be reconstructed, within any desired accuracy, using the Taylor series expansion:

$$\bar{T}(z) = \bar{T}(z_0) + \left.\frac{\partial \bar{T}}{\partial z}\right|_{z=z_0} (z - z_0) + \left.\frac{\partial^2 \bar{T}}{\partial z^2}\right|_{z=z_0} \frac{(z - z_0)^2}{2} + \cdots . \tag{6.2}$$

Hence, it follows that a series of derivatives evaluated at any given point uniquely determine the double-diffusive transport at that location: $F_T = F_T(\partial \bar{T}/\partial z, \partial^2 \bar{T}/\partial z^2, \ldots, \partial \bar{S}/\partial z, \partial^2 \bar{S}/\partial z^2, \ldots)$. In essence, the flux-gradient laws, which assume that fluxes are controlled by $\partial \bar{T}/\partial z$ and $\partial \bar{S}/\partial z$, simply ignore the contribution of the second and higher derivatives in the Taylor series (6.2). Thus, the simplest generalization of the flux-gradient law takes the following form:

$$F_T = \sum_{n=1}^{N} C_{Tn}\frac{\partial^n \bar{T}}{\partial z^n}, \quad F_S = \sum_{n=1}^{N} C_{Sn}\frac{\partial^n \bar{S}}{\partial z^n}, \tag{6.3a,b}$$

where coefficients C_{Tn} and C_{Sn} depend on the density ratio. The next step is based on the axiomatic statement that reversing the direction of the z-axis has no physical consequences for the evolution of any physical system. Therefore, any consistent flux law should be invariant with respect to the transformation

$$(z, F_T, F_S) \rightarrow (-z, -F_T, -F_S). \tag{6.4}$$

In order for the series in (6.3) to satisfy the invariance (6.4) at all spatial locations and instants of time, their even coefficients should be zero:

$$C_{Tn} = C_{Sn} = 0, \quad n = 2, 4, \ldots. \tag{6.5}$$

Thus, the leading-order correction to the flux-gradient model involves not the second derivative (the curvature term) but rather the third one (the aberrancy term). This requirement is reflected in the design of the proposed flux-gradient-aberrancy laws (6.1).

It has recently come to the author's attention that a similar formulation has also been proposed for one-component turbulent mixing (Ruddick 2014). In that study, the aberrancy term was shown to emerge as a result of Gaussian smoothing over the scale of relevant turbulent eddies, effectively eliminating the ultraviolet catastrophe in the Phillips–Posmentier model. It remains to be seen whether the same principle can be adapted for double-diffusive mixing. The successful generalization would offer yet another, perhaps even more physical, argument in support of the double-diffusive flux-gradient-aberrancy laws.

The biharmonic model has been used in the past to surmount numerical difficulties associated with the singularity of the double-diffusive flux-gradient laws as $m \to \infty$ (Radko 2005; Radko *et al.* 2014). However, until now, there has been no guidance with regard to the choice of the aberrancy coefficient μ. As a result, there has been no assurance that the flux-gradient-aberrancy model damps the relevant range of scales. The numerical exploration of the small-scale damping effect in this study, combined with its theoretical rationalization (§§ 4 and 5), opens an attractive opportunity to specify the aberrancy coefficient. The intent in this section is to offer the community a complete – calibrated and tested – closure for modelling of double-diffusively driven fine-scale variability.

The calibration of the new flux laws is based on the linear stability analysis of system (6.1), which results in the following growth-rate equation:

$$\lambda^2 + \lambda m^2 [A_{Nu} + Nu(\bar{\bar{R}}_\rho) - A_\gamma Nu(\bar{\bar{R}}_\rho)\bar{\bar{R}}_\rho - \bar{\bar{R}}_\rho A_{Nu}/\gamma(\bar{\bar{R}}_\rho) - 2\mu m^2] - A_\gamma Nu^2(\bar{\bar{R}}_\rho)\bar{\bar{R}}_\rho m^4$$
$$+ \mu m^6 [A_{Nu} + Nu - A_{Nu}\bar{\bar{R}}_\rho/\gamma(\bar{\bar{R}}_\rho) - A_\gamma Nu(\bar{\bar{R}}_\rho)\bar{\bar{R}}_\rho + \mu m^2] = 0. \tag{6.6}$$

Equation (6.6) represents a generalization of the corresponding flux-gradient equation (2.4) to include selective damping of high wavenumbers; setting the biharmonic coefficient μ to zero makes the two equations identical. The key differences between solutions based on the flux-gradient and flux-gradient-aberrancy models are illustrated in figure 9. Here we plot the largest growth rates obtained using (2.4) and (6.6) as a function of vertical wavelength for $\mu = 3000$. The two models are close for $H > 300$, but the agreement rapidly deteriorates for smaller wavelengths. Importantly, the flux-gradient-aberrancy model offers an adequate description of the DNS-based estimates (figure 6) at all scales – something that the flux-gradient laws fail to accomplish.

The series of DNS in figure 8(*b*), as well as the supporting analytical arguments in §4, indicate that the range of validity of the flux-gradient model is rather insensitive to the background density ratio. For all values of $\bar{\bar{R}}_\rho$, the growth rate changes sign at $H_0 \approx 150$. This observation makes it possible to evaluate the relevant values of μ by insisting that $(\lambda, m) = (0, 2\pi/H_0)$ satisfies the growth-rate equation (6.6). The resulting estimate of μ is plotted as a function of $\bar{\bar{R}}_\rho$ in figure 10. The biharmonic coefficient rapidly decreases with the density ratio and can be approximated by the exponential relation

$$\mu = a_\mu \exp(b_\mu \bar{\bar{R}}_\rho), \quad (a_\mu, b_\mu) = (4.433 \times 10^4, -1.696), \tag{6.7a,b}$$
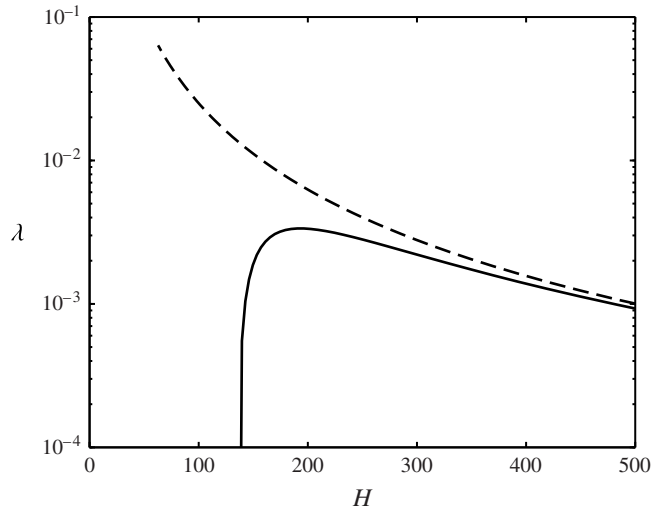
as shown in figure 10.

FIGURE 9. The growth rate of layering modes (λ) as a function of their wavelength (H). The solid curve represents the estimate obtained using the flux-gradient-aberrancy law (6.1) with $\mu = 3000$ and the corresponding estimate obtained using the flux-gradient model (2.3) is indicated by the dashed curve. The two estimates are consistent for long wavelengths but rapidly diverge as H decreases.
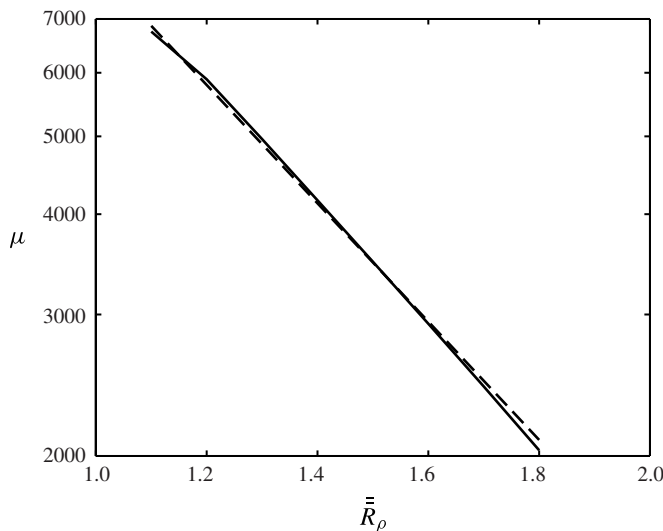

FIGURE 10. Calibration of the biharmonic coefficient μ. For each value of $\bar{\bar{R}}_\rho$, the coefficient μ is evaluated by insisting that the layering growth rate λ is zero for $H = 150$ (regardless of the density ratio). The resulting dependence (solid curve) is plotted along with the empirical approximation (6.7) indicated by the dashed line.

6.2. *One-dimensional modelling*

It is of interest to examine some one-dimensional (z) numerical solutions based on the flux-gradient-aberrancy model. Our governing equations are represented
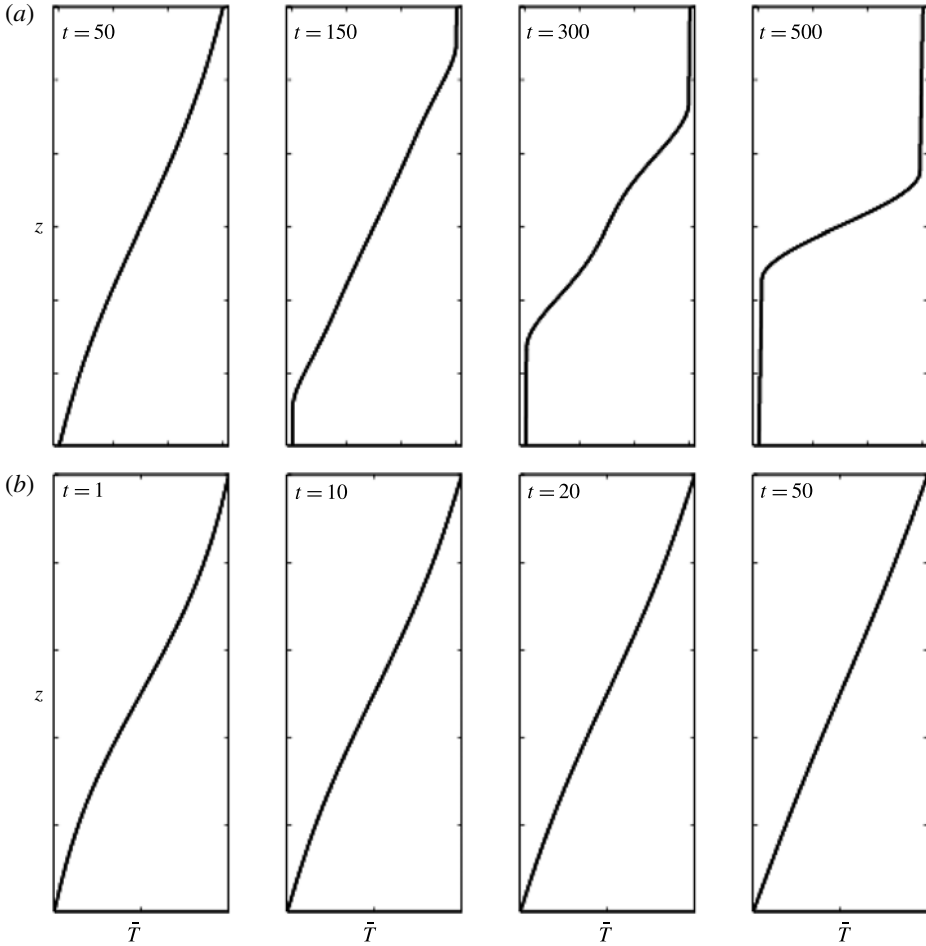
FIGURE 11. One-dimensional solutions of the flux-gradient-aberrancy model (6.1). (*a*) The evolution of temperature profile in the experiment with $\bar{\bar{R}}_\rho = 1.5$, $\mu = 3480$ and $H = 300$. (*b*) The experiment in (*a*) is reproduced with $H = 100$. The reduction in vertical extent dramatically alters the stability characteristics of the system.

by (6.1) for regions susceptible to fingering $(\partial \bar{\rho}/\partial z < 0)$, whereas for convective conditions $(\partial \bar{\rho}/\partial z > 0)$ we assume uniform and equal diffusivities of heat and salt $(K_T = K_S = 5000)$. The resulting system was integrated numerically in time using the pseudospectral method described and used by Radko (2005). Figure 11(*a*) presents an experiment initiated by a small-amplitude fundamental harmonic with wavelength $H = 300$. As expected, the perturbation grows monotonically at the rate consistent with gamma-instability theory, eventually transforming the system into two well-mixed convecting layers separated by thin fingering interface. The equilibrium thickness of the interface in this simulation is $h = 51$. A very different scenario is realized in the experiment shown in figure 11(*b*). The experimental set-up is the same as in figure 11(*a*), but the wavelength is significantly lower: $H = 100$. In this case, the initial perturbation rapidly decays and the final state represents a uniformly stratified temperature and salinity stratifications.
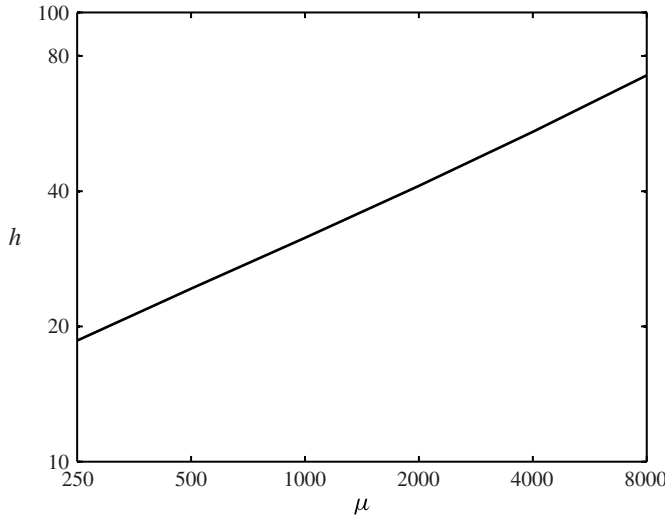
FIGURE 12. Diagnostics of one-dimensional simulations using the flux-gradient-aberrancy model (6.1). The equilibrium thickness h of fingering interface is plotted as a function of the assumed biharmonic coefficient μ in logarithmic coordinates.

A largely unresolved problem in the theory of double-diffusive convection concerns the equilibrium thickness of fingering interfaces in thermohaline staircase. Our simple one-dimensional model offers some insight into the selection of the interfacial thickness h. Figure 12 presents the values of h diagnosed from a series of simulations in which the biharmonic coefficient was systematically varied from $\mu = 250$ to $\mu = 8000$. All simulations were initiated by two initially homogeneous layers separated by a discontinuous interface. In time, the interfaces diffused to equilibrium values. The interfacial thickness in each experiment was defined as $h = \Delta T / \max(\bar{T}_z)$, where $\max(\bar{T}_z)$ is the maximal temperature gradient (typically found at the centre of an interface) and ΔT is the temperature difference between the well-mixed layers. The results in figure 12 suggest a distinct, rapidly increasing, dependence of h on μ. The numerical data points align in the logarithmic coordinates along a straight line, which indicates that the $h(\mu)$ relation can be accurately approximated by the simple power law

$$h = a_h \mu^{b_h}, \quad (a_h, b_h) = (2.03, 0.40). \quad (6.8a,b)$$

The exponent of this power law is somewhat different from $b_h = 1/2$, which could have been expected from the structure of the flux-gradient-aberrancy equations (6.6). The difference in the exponents is likely to be the result of processes involved in the interaction between fingering and convective regions. Extrapolation of (6.8) to small values of μ implies that the interfacial thickness inexorably reduces to zero in the limit $\mu \to 0$. This, in turn, suggests that the processes controlling interfacial thickness are closely related to the point-of-failure effect.

Finally, it behooves us to compare the structure and dimensions of fingering interfaces predicted by the flux-gradient model with the corresponding simulations and field measurements. Therefore, figure 13(a) presents the mean temperature profile for the DNS in figure 5. This profile was obtained by averaging the DNS-generated temperature fields in x and t over the period following the formation of a well-defined step and its statistical equilibration. This profile is close to the corresponding
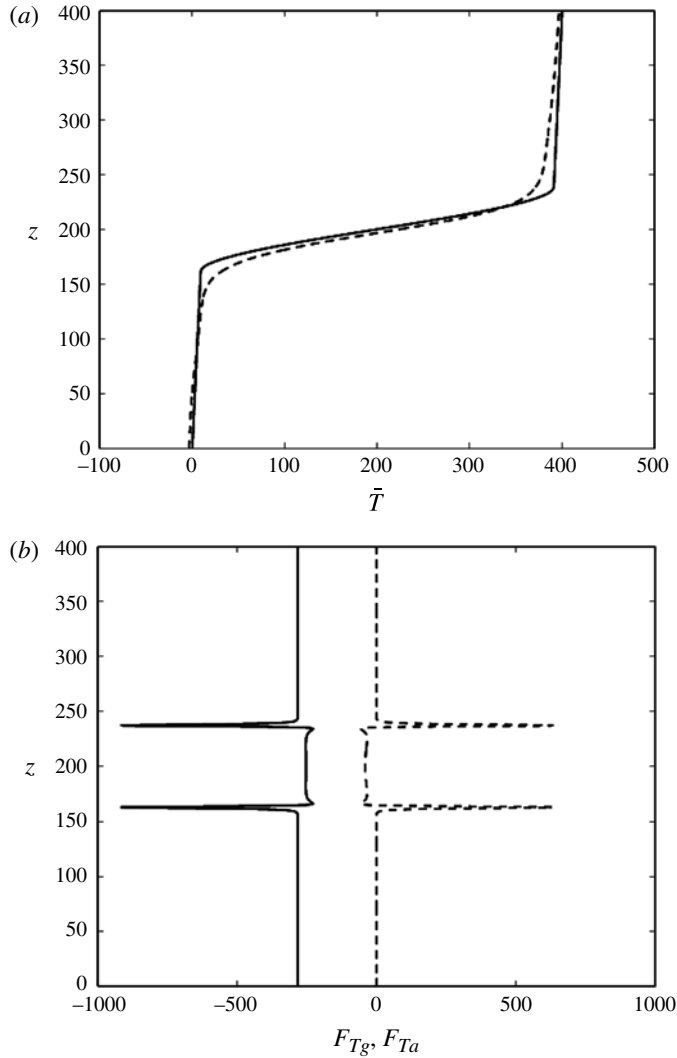
FIGURE 13. (*a*) Comparison of the final mean temperature profile realized in the DNS experiment shown in figure 5 (dashed curve) with the corresponding prediction of the flux-gradient-aberrancy model (solid curve). (*b*) The vertical profiles of the gradient (solid curve) and aberrancy (dashed curve) components of the temperature flux in the flux-gradient-aberrancy model.

prediction of the flux-gradient-aberrancy model, also shown in figure 13(*a*). The agreement is particularly impressive in the interior of the interface, implying that the model is highly successful in predicting the interfacial gradients. Some quantitative differences can be observed near the edges of the interface, which suggests that the flux-gradient-aberrancy models can be further improved to capture the dynamics of the matching regions, separating the finger zones from the adjacent convecting layers.

Figure 13(*b*) presents the vertical distribution of the two flux components, i.e. the gradient flux $F_{T,g} = -Nu \, \partial \bar{T}/\partial z$ and the aberrancy flux $F_{T,a} = \mu \, \partial^3 \bar{T}/\partial z^3$. These components vary in a compensating manner, since in the equilibrated state their
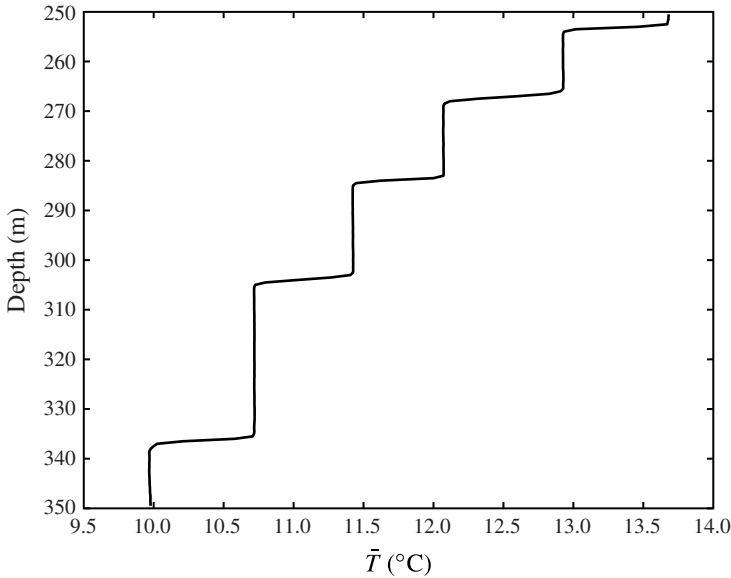
FIGURE 14. One of the temperature profiles taken through the Caribbean staircase during the Salt Finger Tracer Release Experiment (modified from figure 1(a) in Schmitt *et al.* (2005)).

sum is vertically uniform. The largest variability is associated with the transition from fingering to convective regimes at the edges of the interface. It is interesting that, despite the utmost significance of the aberrancy term for interfacial dynamics, numerically the average vertical fluxes in interfaces are clearly dominated by their gradient components. For the calculation in figure 13, the ratio of the average gradient temperature flux in the interface to the corresponding aberrancy flux is $\langle F_{T,g} \rangle / \langle F_{T,a} \rangle \approx 6.6$. The gradient/aberrancy flux ratio is even larger for salinity: $\langle F_{S,g} \rangle / \langle F_{S,a} \rangle \approx 23.2$. These findings suggest that the heat and salt diffusivities evaluated locally in relatively thin interfaces are comparable to the diffusivities realized in effectively unbounded gradients for the same values of $\bar{R}_\rho$.

Finally, we attempt to validate the flux-gradient-aberrancy model using oceanographic observations. The following comparison is based on a typical vertical temperature profile (figure 14) taken through the Caribbean staircase during the Salt Finger Tracer Release Experiment (Schmitt *et al.* 2005). Figure 14 presents the profile section at the 250–350 m depth range, which contains five well-defined steps (data courtesy of Ray Schmitt). In order to compare the model prediction with these observations, we have run five one-step simulations using the flux-gradient-aberrancy model – one for each interface in figure 14. In these calculations, the background field $(\bar{\bar{T}}_{z,dim}, \bar{\bar{S}}_{z,dim})$ was defined based on the parameters of a region extending from the centre of the mixed layer above the simulated interface to the centre of the layer below. Each simulation was initiated by homogeneous layers separated by a discontinuous jump in temperature and salinity. The initial stage of each simulation was characterized by the vertical spreading of interfaces due to the action of the aberrancy term. The time integrations were carried on until the systems reached full equilibration. For ease of comparison, the final steady states of these simulations were referenced to the depth and temperature of the corresponding observations and plotted together
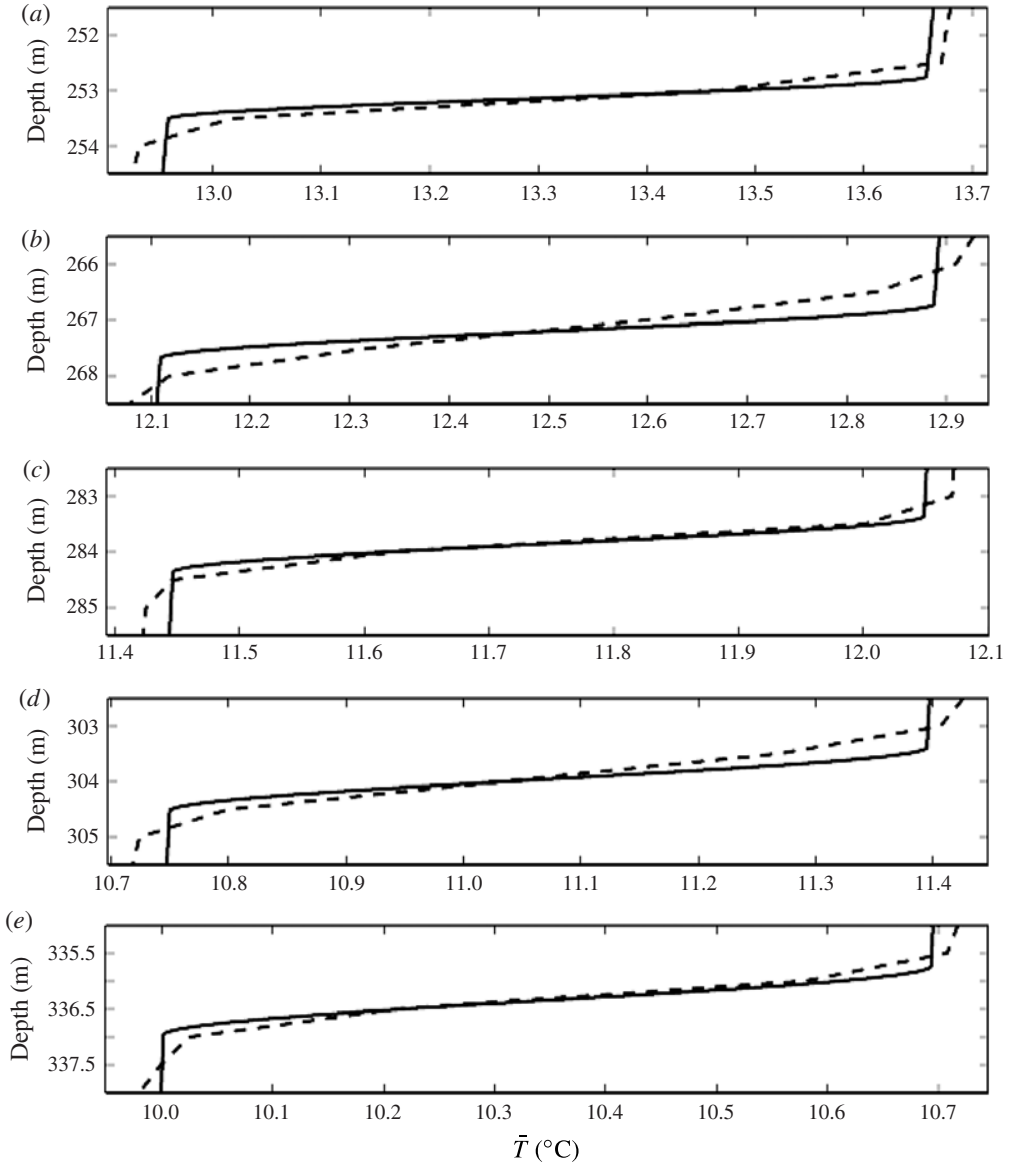
FIGURE 15. Temperature patterns in the observed interfaces shown in figure 14 (dashed curves) are compared with the corresponding predictions of the flux-gradient-aberrancy model (solid curves).

in figure 15. The agreement of the flux-gradient-aberrancy model with observations is understandably worse than with the DNS (figure 13a) but still encouraging. In all simulations the interfacial thickness is systematically underestimated, albeit only by a factor of 2 or less. This difference should not necessarily be attributed to the deficiencies of the flux-gradient-aberrancy model, since the oceanic environment is home to many processes that the model is not meant to represent. These elements include mechanically generated turbulence due to overturning internal waves, strong

shears, and active mesoscale and sub-mesoscale variability, all of which could lead to thickening of the observed interfaces.

Finally, it should be noted that the system (6.1) is written in terms of non-dimensional variables and the system of non-dimensionalization is based on the overall background gradients. Therefore, our flux model is implicitly non-local – the dimensional transport values at given depth depend not only on the local conditions but also on the mean background stratification. It is not clear whether the assumed non-locality is realistic or whether it represents an artifact of the model formulation. Therefore, in appendix B we present a purely local, albeit somewhat more complicated, version of the flux-gradient-aberrancy model (6.1).

7. Discussion

The most common and, so far, the most effective approach to the analysis of secondary double-diffusive structures – staircases, thermohaline intrusions and collective instability waves – is based on the application of flux-gradient laws, which assume a unique relation between the finger-driven T–S transport and vertical property gradients. Models based on flux-gradient laws adequately describe the dynamics of large-scale (relative to individual fingers) phenomena. However, such models are known to develop unphysical behaviour at small scales, which severely limits their implementation and predictive capabilities.

The objective of this study is two-fold: (i) the formulation of an explicit analytical model for the point of failure of the flux-gradient laws and (ii) the development of an alternative mixing parametrization, capable of representing secondary double-diffusive phenomena at all scales. The specific problem chosen for the analysis of the point-of-failure effect and for testing new parametrizations is that of spontaneous layering in a uniform finger-favourable stratification. This choice is easy to justify: the failure of flux-gradient laws at small scales is most evident for the layering problem and its consequences are profound. Layering solutions, obtained using the flux-gradient model, suffer from ultraviolet catastrophe – an unbounded increase in the growth rates of unstable modes with decreasing wavelength. While it is generally accepted that finger/layer scale separation is essential for the applicability of the flux-gradient laws, the quantification of this requirement, particularly from first principles, is problematic. The key difficulty here is that the flux-gradient laws themselves offer no guidance with regard to their range of validity. Therefore, we have also examined the layering problem using the techniques of multiscale analysis based on the Kolmogorov background state, representing a series of vertically oriented salt fingers.

The multiscale and flux-gradient models are analogous in many respects. However, owing to its explicit character, the multiscale model makes it possible to identify the range of scales where the lack of scale separation has an adverse impact on the model's fidelity. This is accomplished by comparing asymptotic multiscale solutions with their finite-amplitude counterparts, which make no assumption about the scale separation. The significant difference between the two models at small scales is interpreted as a sign that the lack of scale separation between fingers and layering modes affects the system dynamics. This criterion is used to establish the range of validity for the flux-gradient models. Our theory suggests that the effects associated with the proximity of finger and layering scales come into play at wavelengths of $H_{pof} \sim 200$–300, with rather limited variation in H_{pof} with the background density ratio. In dimensional units, evaluated for typical stratification in the mid-latitude thermocline, this estimate corresponds to $H_{pof,dim} \sim 2.5$ m. These theoretical inferences have been

supported by a series of DNS (§ 5), which indicate that, for scales exceeding H_{pof}, the growth rates evaluated with the flux-gradient theory closely match the numerically derived counterparts. For $H < H_{pof}$, the flux-gradient model becomes largely irrelevant.

Of course, the interest in the multiscale double-diffusive model is not limited to the assessment of the applicability of the flux-gradient laws. Perhaps an even broader theoretical significance of multiscale analyses lies in their ability to adequately represent a remarkably wide range of layering phenomena. Multiscale solutions have been used to conceptualize dynamics of planetary jets, generated and maintained by mesoscale variability (Manfroi & Young 1999, 2002), layering forced by small-scale turbulence in stratified one-component fluids (Balmforth & Young 2002, 2005), thermohaline interleaving driven by lateral property gradients (Radko 2011) and, in this study, the formation of double-diffusive staircases. Their ability to explain the physics of such dissimilar systems is truly remarkable, and this investigation is yet another testament to the power and generality of multiscale modelling. The multiscale double-diffusive model captures such subtle effects as the control of thermohaline layering by the variation in flux ratio and the selection of the point-of-failure scale. In contrast, the Phillips–Posmentier anti-diffusive mixing model – another commonly used conceptualization – is surprisingly limited in representing the dynamics of double-diffusive layering (§ 2.1).

The theoretical model in § 4 also offers important insights into the specific mechanisms responsible for the failure of the flux-gradient laws. It suggests that the system of vertically elongated fingers becomes linearly stable with respect to horizontally uniform modes at sufficiently small scales. This small-scale stabilization effect is not captured by flux-gradient models, which are not designed to explicitly reflect the microscale dynamics of salt fingers. As a result, they erroneously predict the rapid growth of small-scale modes. While this explanation is plausible and our theoretical estimates of the point-of-failure scale are consistent with simulations, it is possible that other mechanisms could also play a role in the failure of flux-gradient laws. For instance, the model of layering in one-component flows (Balmforth, Llewellyn Smith & Young 1998) emphasizes the significance of the interplay between the buoyancy stratification and the turbulent kinetic energy. These dynamics result in the delayed response of the vertical fluxes to changes in stratification and ultimately stabilize modes with small wavelength. Undoubtedly, certain delay in the adjustment of fluxes is bound to occur in double-diffusive systems as well and it is not captured by the extant flux-gradient laws. This deficiency could also potentially contribute to their failure at small scales.

A more constructive and practical objective of this study is to offer a simple remedy for extant double-diffusive parametrizations – the flux-gradient-aberrancy laws (6.1). These laws incorporate, in addition to gradients, dependence on the third-order derivatives of large-scale properties (the aberrancy terms), which removes the aforementioned limitations of flux-gradient parametrizations. The aberrancy coefficient μ was calibrated by requiring that the model solutions be consistent with layering DNS and with the point-of-failure theory. We show that the one-dimensional layered solutions obtained using the flux-gradient-aberrancy laws capture the main features of oceanic thermohaline staircases. For instance, one of the unresolved questions in the staircase theory concerns the thickness of fingering interfaces, sandwiched between well-mixed convecting layers. Our numerical experiments with the flux-gradient-aberrancy model indicate that the interfacial thickness is directly controlled by the aberrancy terms, becoming infinitesimally small in the limit $\mu \to 0$. These terms represent the point-of-failure effect, manifested by selective damping of

relatively small scales. Hence, we propose that the interfacial thickness is set by a balance between two adverse processes: convective overturning in the mixed layers, which acts to reduce the size of the fingering zone, and the tendency of the interface to spread vertically due to the aberrancy effect.

This possibility leads to an interesting and unorthodox suggestion that the interfacial thickness in thermohaline staircases is ultimately set by the point-of-failure scale (H_{pof}) – the subject of our current investigation. Our preliminary attempts to apply these ideas to oceanic staircases are encouraging. For instance, we can assume that the non-dimensional interfacial thickness scales as $h \sim H_{pof} \sim 300$, as suggested by DNS and by the point-of-failure theory (§§ 4 and 5). Upon dimensionalization, we obtain $h_{dim} \sim 2$ m for the Caribbean staircase and $h_{dim} \sim 6$ m for the staircase in the western Mediterranean. These numbers come tantalizingly close to the observations summarized in table 1. The ideas advocated in this study imply that the thickness of high-gradient interfaces in fully developed staircases is ultimately set by Stern's (1960) nominal finger scale $l = (k_T \nu / g\alpha \bar{\bar{T}}_z)^{1/4}$ with a rather large prefactor ($\sim$300).

Finally, it is emphasized that the problem of failure of the flux-gradient laws is examined here on an important but perhaps somewhat special problem – spontaneous layering in an initially homogeneous stratification. However, it is our belief that the analysis presented here is of much broader relevance and that the proposed flux-gradient-aberrancy laws can benefit the modelling of other fine-scale double-diffusive processes. Testing this proposition is left for future studies.

Acknowledgements

Appendix A. Gamma-effect in the multiscale model

The leading-order balances of the T–S equations for the linear growing modes identified by the multiscale model of § 3 can be expressed as

$$
\begin{cases}
\lambda_{ms} T_0 + \dfrac{\partial}{\partial z}(F_{T,bg} + F'_T) = 0, \\[2mm]
\lambda_{ms} S_0 + \dfrac{\partial}{\partial z}(F_{S,bg} + F'_S) = 0,
\end{cases}
\tag{A 1}
$$

where

$$
F_{T,bg} = -\tfrac{1}{2}\hat{T}_{bg}\hat{\psi}_{bg}k - 1 \quad \text{and} \quad F_{S,bg} = -\tfrac{1}{2}\hat{S}_{bg}\hat{\psi}_{bg}k - \tau\bar{\bar{R}}_\rho
\tag{A 2a,b}
$$

are the horizontally averaged fluxes of heat and salt associated with the background state, and

$$
F'_T = -\frac{1}{2}(\hat{T}_{bg}\psi_{1A} + T_{1B}\hat{\psi}_{bg})k - \frac{\partial T_0}{\partial z} \quad \text{and} \quad F'_S = -\frac{1}{2}(\hat{S}_{bg}\psi_{1A} + S_{1B}\hat{\psi}_{bg})k - \tau\frac{\partial S_0}{\partial z}
\tag{A 3a,b}
$$

are the fluxes associated with the harmonic perturbation (3.13).

After linearization, the flux ratio is written as

$$\gamma \approx \frac{F_{T,bg} + F'_T}{F_{S,bg} + F'_S} \approx \gamma_{bg} + \gamma', \tag{A4}$$

where

$$\gamma_{bg} = \frac{F_{T,bg}}{F_{S,bg}} \tag{A5}$$

is the background flux ratio, and the perturbation takes the form

$$\gamma' = \frac{F_{T,bg}}{F_{S,bg}} \left(\frac{F'_T}{F_{T,bg}} - \frac{F'_S}{F_{S,bg}} \right). \tag{A6}$$

Similarly, we linearize the expression for the local, horizontally averaged, density ratio:

$$\bar{R}_\rho \approx \frac{1 + \dfrac{\partial T_0}{\partial z}}{\dfrac{1}{\bar{\bar{R}}_0} + \dfrac{\partial S_0}{\partial z}} \approx \bar{\bar{R}}_0 + \bar{\bar{R}}_0 \left(\frac{\partial T_0}{\partial z} - \bar{\bar{R}}_0 \frac{\partial S_0}{\partial z} \right). \tag{A7}$$

Combining (A 1) with (A 4) results in

$$\lambda_{ms}(T_0 - \gamma_{bg} S_0) + \frac{\partial \gamma}{\partial z} F_{S,bg} = 0. \tag{A8}$$

In order to emphasize the link between the multiscale and flux-gradient theories, the vertical derivative of the flux ratio in (A 8) is expressed in terms of its $\bar{R}_\rho$ derivative as

$$\frac{\partial \gamma}{\partial z} = \frac{\partial \gamma}{\partial \bar{R}_\rho} \frac{\partial \bar{R}_\rho}{\partial z}, \tag{A9}$$

which is further modified using (A 7) as follows:

$$\frac{\partial \gamma}{\partial z} = \frac{\partial \gamma}{\partial \bar{R}_\rho} \bar{\bar{R}}_0 \left(\frac{\partial^2 T_0}{\partial z^2} - \bar{\bar{R}}_0 \frac{\partial^2 S_0}{\partial z^2} \right). \tag{A10}$$

Finally, combining (A 8) with (A 10), we arrive at

$$\lambda_{ms} = -\frac{\partial \gamma}{\partial \bar{R}_\rho} \frac{\bar{\bar{R}}_\rho F_{S,bg} \left(\dfrac{\partial^2 T_0}{\partial z^2} - \bar{\bar{R}}_0 \dfrac{\partial^2 S_0}{\partial z^2} \right)}{2(T_0 - \gamma_{bg} S_0)}. \tag{A11}$$

Equation (3.16), discussed in §3, is obtained from (A 11) by expressing (T_0, S_0) in terms of modal amplitudes and vertical wavenumber using (3.13).

Appendix B. The local version of the flux-gradient-aberrancy laws

The dimensional form of the flux-gradient-aberrancy laws (6.1) can be written as

$$
\begin{cases}
\dfrac{\partial \bar{T}_{dim}}{\partial t_{dim}} = k_T \dfrac{\partial}{\partial z_{dim}} \left(Nu(\bar{R}_\rho) \dfrac{\partial \bar{T}_{dim}}{\partial z_{dim}} \right) - k_T \sqrt{\dfrac{k_T \nu}{g \alpha \bar{\bar{T}}_{z,dim}}} \mu(\bar{\bar{R}}_\rho) \dfrac{\partial^4 \bar{T}_{dim}}{\partial z_{dim}^4}, \\[4mm]
\dfrac{\partial \bar{S}_{dim}}{\partial t_{dim}} = k_T \dfrac{\partial}{\partial z_{dim}} \left(\dfrac{Nu(\bar{R}_\rho)}{\gamma(\bar{R}_\rho)} \dfrac{\partial \bar{T}_{dim}}{\partial z_{dim}} \right) - k_T \sqrt{\dfrac{k_T \nu}{g \alpha \bar{\bar{T}}_{z,dim}}} \mu(\bar{\bar{R}}_\rho) \dfrac{\partial^4 \bar{S}_{dim}}{\partial z_{dim}^4},
\end{cases}
\tag{B 1}
$$

which reveals that T–S fluxes are determined by both the local stratification and the background gradients $(\bar{\bar{T}}_{z,dim}, \bar{\bar{S}}_{z,dim})$. The obvious advantage of this system lies in its simplicity – the linearity of the aberrancy term affords analytical and numerical treatments of (B 1) that would be unsuitable for more complicated representations of small-scale damping. However, the assumed dependence of the local transport on the global characteristics of the system may appear somewhat counterintuitive. Therefore, we also propose a straightforward adjustment of (B 1) that transforms it into a fully local closure:

$$
\begin{cases}
\dfrac{\partial \bar{T}_{dim}}{\partial t_{dim}} = k_T \dfrac{\partial}{\partial z_{dim}} \left(Nu(\bar{R}_\rho) \dfrac{\partial \bar{T}_{dim}}{\partial z_{dim}} \right) - k_T \sqrt{\dfrac{k_T \nu}{g \alpha \bar{T}_{z,dim}}} \mu(\bar{R}_\rho) \dfrac{\partial^4 \bar{T}_{dim}}{\partial z_{dim}^4}, \\[4mm]
\dfrac{\partial \bar{S}_{dim}}{\partial t_{dim}} = k_T \dfrac{\partial}{\partial z_{dim}} \left(\dfrac{Nu(\bar{R}_\rho)}{\gamma(\bar{R}_\rho)} \dfrac{\partial \bar{T}_{dim}}{\partial z_{dim}} \right) - k_T \sqrt{\dfrac{k_T \nu}{g \alpha \bar{T}_{z,dim}}} \mu(\bar{R}_\rho) \dfrac{\partial^4 \bar{S}_{dim}}{\partial z_{dim}^4}.
\end{cases}
\tag{B 2}
$$

The distinction between (B 1) and (B 2) is limited to replacing the background gradients in the aberrancy coefficient by the corresponding local values. Importantly, this modification does not require recalibration of the aberrancy coefficient (6.7) since this expression was obtained on the basis of numerical stability analyses of linear mean T–S gradients.

However, important differences appear in the final nonlinear step-like solutions obtained using local and non-local formulations. For instance, scaling analysis of the non-local parametrization (B 1) for thin high-gradient interfaces (Radko 2005) suggests that the interfacial fluxes are proportional to the cross-interfacial temperature variation: $F_{T,dim} \propto \Delta T_{dim}$. This result obviously contradicts the well-known 4/3 flux law (Turner 1967). The inconsistency between these results is not surprising. The key assumption of Turner's theory is that the fluxes are uniquely determined by the cross-interfacial T–S jumps and are independent of (say) the thickness of convecting layers. This assumption clearly does not hold for the non-local closure (B 1).

In order to examine whether the local parametrization (B 2) conforms to the 4/3 law, we consider a fully equilibrated interface, in which case its gradient and aberrancy components are compensating:

$$
k_T \dfrac{\partial}{\partial z_{dim}} \left(Nu(\bar{R}_\rho) \dfrac{\partial \bar{T}_{dim}}{\partial z_{dim}} \right) \sim k_T \sqrt{\dfrac{k_T \nu}{g \alpha \bar{T}_{dim,z}}} \mu(\bar{R}_\rho) \dfrac{\partial^4 \bar{T}_{dim}}{\partial z_{dim}^4}.
\tag{B 3}
$$

Scaling (B 3) in terms of interfacial temperature variation ΔT_{dim} and interfacial thickness Δh_{dim} yields

$$
\dfrac{\Delta T_{dim}}{h_{dim}^2} \propto \sqrt{\dfrac{h_{dim}}{\Delta T_{dim}}} \dfrac{\Delta T_{dim}}{h_{dim}^4} \quad \rightarrow \quad h_{dim} \propto \Delta T_{dim}^{-1/3}.
\tag{B 4}
$$

Using (B 4), we scale the cross-interfacial flux as follows:

$$F_{T,dim} \propto \frac{\Delta T_{dim}}{h_{dim}} \propto \Delta T_{dim}^{4/3}, \qquad \text{(B 5)}$$

arriving at the 4/3 flux law.

The consistency of (B 2) with Turner's flux law should not be interpreted as a sign of its superiority over the non-local form (B 1). The applicability of the 4/3 flux law to fingering interfaces is a controversial subject. Numerous attempts to evaluate the exponent of the interfacial flux laws on the basis of numerical and laboratory experiments have produced rather ambiguous results (see table 4.1 in Radko 2013). The existing experimental and numerical evidence appears insufficient to either confirm or rule out the 4/3 law for salt-finger interfaces, and its applicability to the oceanic staircases is even more questionable (Kunze 1987). Given the current uncertainties, it is perhaps reasonable to recommend utilizing a simpler non-local closure.

REFERENCES

BALMFORTH, N. J., LLEWELLYN SMITH, S. G. & YOUNG, W. R. 1998 Dynamics of interfaces and layers in a stratified turbulent fluid. *J. Fluid Mech.* **355**, 329–358.

BALMFORTH, N. J. & YOUNG, Y.-N. 2002 Stratified Kolmogorov flow. *J. Fluid Mech.* **450**, 131–167.

BALMFORTH, N. J. & YOUNG, Y.-N. 2005 Stratified Kolmogorov flow. Part 2. *J. Fluid Mech.* **528**, 23–42.

BRYDEN, H. L., SCHROEDER, K., SPARNOCCHIA, S., BORGHINI, M. & VETRANO, A. 2014 Thermohaline staircases in the western Mediterranean Sea. *J. Mar. Res.* (in press).

GAMA, S., VERGASSOLA, M. & FRISCH, U. 1994 Negative eddy viscosity in isotropically forced two-dimensional flow – linear and nonlinear dynamics. *J. Fluid Mech.* **260**, 95–126.

GARGETT, A. E. & SCHMITT, R. W. 1982 Observations of salt fingers in the central waters of the eastern North Pacific. *J. Geophys. Res.* **87**, 8017–8092.

HOLYER, J. Y. 1981 On the collective instability of salt fingers. *J. Fluid Mech.* **110**, 195–207.

HOLYER, J. Y. 1984 The stability of long, steady, two-dimensional salt fingers. *J. Fluid Mech.* **147**, 169–185.

HOLYER, J. Y. 1985 The stability of long steady three-dimensional salt fingers to long wavelength perturbations. *J. Fluid Mech.* **156**, 495–503.

KELLEY, D. E., FERNANDO, H. J. S., GARGETT, A. E., TANNY, J. & OZSOY, E. 2003 The diffusive regime of double-diffusive convection. *Prog. Oceanogr.* **56**, 461–481.

KIMURA, S. & SMYTH, W. D. 2007 Direct numerical simulation of salt sheets and turbulence in a double-diffusive shear layer. *Geophys. Res. Lett.* **34**, L21610.

KRISHNAMURTI, R. 2003 Double-diffusive transport in laboratory thermohaline staircases. *J. Fluid Mech.* **483**, 287–314.

KUNZE, E. 1987 Limits on growing, finite length salt fingers: a Richardson number constraint. *J. Mar. Res.* **45**, 533–556.

KUNZE, E. 2003 A review of salt fingering theory. *Prog. Oceanogr.* **56**, 399–417.

LEGRAS, B. & VILLONE, B. 2009 Large-scale instability of a generalized turbulent Kolmogorov flow. *Nonlinear Process. Geophys.* **16**, 569–577.

LINDEN, P. F. 1974 Salt fingers in a steady shear flow. *Geophys. Fluid Dyn.* **6**, 1–27.

MANFROI, A. & YOUNG, W. 1999 Slow evolution of zonal jets on the beta plane. *J. Atmos. Sci.* **56**, 784–800.

MANFROI, A. & YOUNG, W. 2002 Stability of beta-plane Kolmogorov flow. *Physica* D **162**, 208–232.

MEI, C. C. & VERNESCU, M. 2010 *Homogenization Methods for Multiscale Mechanics.* p. 330. World Scientific.

MERRYFIELD, W. J. 2000 Origin of thermohaline staircases. *J. Phys. Oceanogr.* **30**, 1046–1068.

MESHALKIN, L. & SINAI, Y. 1961 Investigation of the stability of a stationary solution of a system of equations for the plane movement of an incompressible viscous fluid. *J. Appl. Math. Mech.* **25**, 1700–1705.

MIROUH, G. M., GARAUD, P., STELLMACH, S., TRAXLER, A. L. & WOOD, T. S. 2012 A new model for mixing by double-diffusive convection (semi-convection). I. The conditions for layer formation. *Astrophys. J.* **750**, 61.

MUELLER, R. D., SMYTH, W. D. & RUDDICK, B. 2007 Shear and convective turbulence in a model of thermohaline intrusions. *J. Phys. Oceanogr.* **37**, 2534–2549.

NOVIKOV, A. & PAPANICOLAU, G. 2001 Eddy viscosity of cellular flows. *J. Fluid Mech.* **446**, 173–198.

PHILLIPS, O. M. 1972 Turbulence in a strongly stratified fluid is it unstable? *Deep-Sea Res.* **19**, 79–81.

POSMENTIER, E. S. 1977 The generation of salinity fine structure by vertical diffusion. *J. Phys. Oceanogr.* **7**, 298–300.

RADKO, T. 2003 A mechanism for layer formation in a double-diffusive fluid. *J. Fluid Mech.* **497**, 365–380.

RADKO, T. 2005 What determines the thickness of layers in a thermohaline staircase? *J. Fluid Mech.* **523**, 79–98.

RADKO, T. 2008 The double-diffusive modon. *J. Fluid Mech.* **609**, 59–85.

RADKO, T. 2011 Mechanics of thermohaline interleaving: beyond the empirical flux laws. *J. Fluid Mech.* **675**, 117–140.

RADKO, T. 2013 *Double-Diffusive Convection*. p. 344. Cambridge University Press.

RADKO, T., BULTERS, A., FLANAGAN, J. & CAMPIN, J.-M. 2014 Double-diffusive recipes. Part 1: Large-scale dynamics of thermohaline staircases. *J. Phys. Oceanogr.* **44**, 1269–1284.

RADKO, T. & SMITH, D. P. 2012 Equilibrium transport in double-diffusive convection. *J. Fluid Mech.* **692**, 5–27.

RADKO, T. & STERN, M. E. 2011 Finescale instabilities of the double-diffusive shear flow. *J. Phys. Oceanogr.* **41**, 571–585.

RUDDICK, B. R., MCDOUGALL, T. J. & TURNER, J. S. 1989 The formation of layers in a uniformly stirred density gradient. *Deep-Sea Res.* **36**, 597–609.

RUDDICK, B. 1997 Differential fluxes of heat and salt: implications for circulation and ecosystem modelling. *Oceanography* **10**, 122–127.

RUDDICK, B. 2014 On the scale of layers formed in strongly stratified turbulent mixing. Unpublished manuscript.

RUDDICK, B. & KERR, O. 2003 Oceanic thermohaline intrusions: theory. *Prog. Oceanogr.* **56**, 483–497.

SCHMITT, R. W. 1979a The growth rate of supercritical salt fingers. *Deep-Sea Res.* **26A**, 23–44.

SCHMITT, R. W. 1979b Flux measurements on salt fingers at an interface. *J. Mar. Res.* **37**, 419–436.

SCHMITT, R. W. 1994 Double diffusion in oceanography. *Annu. Rev. Fluid Mech.* **26**, 255–285.

SCHMITT, R. W. 2003 Observational and laboratory insights into salt finger convection. *Prog. Oceanogr.* **56**, 419–433.

SCHMITT, R. W., LEDWELL, J. R., MONTGOMERY, E. T., POLZIN, K. L. & TOOLE, J. M. 2005 Enhanced diapycnal mixing by salt fingers in the thermocline of the tropical Atlantic. *Science* **308**, 685–688.

SHEN, C. Y. & SCHMITT, R. W. 1995 The wavenumber spectrum of salt fingers. In *Double-Diffusive Convection* (ed. A. Brandt & H. Fernando), AGU Geophysical Monograph, vol. 94, pp. 305–312. American Geophysical Union.

SIVASHINSKY, G. 1985 Weak turbulence in periodic flows. *Physica* D **17**, 243–255.

SMYTH, W. D. & RUDDICK, B. 2010 Effects of ambient turbulence on interleaving at a baroclinic front. *J. Phys. Oceanogr.* **40**, 685–712.

STELLMACH, S., TRAXLER, A., GARAUD, P., BRUMMELL, N. & RADKO, T. 2011 Dynamics of fingering convection. II: The formation of thermohaline staircases. *J. Fluid Mech.* **677**, 554–571.

STERN, M. E. 1960 The 'salt-fountain' and thermohaline convection. *Tellus* **12**, 172–175.

STERN, M. E. 1967 Lateral mixing of water masses. *Deep-Sea Res.* **14**, 747–753.

STERN, M. E., RADKO, T. & SIMEONOV, J. 2001 3D salt fingers in an unbounded thermocline with application to the Central Ocean. *J. Mar. Res.* **59**, 355–390.

STERN, M. E. & SIMEONOV, J. 2002 Internal wave overturns produced by salt fingers. *J. Phys. Oceanogr.* **32**, 3638–3656.

TRAXLER, A., STELLMACH, S., GARAUD, P., RADKO, T. & BRUMMEL, N. 2011 Dynamics of fingering convection. I: Small-scale fluxes and large-scale instabilities. *J. Fluid Mech.* **677**, 530–553.

TURNER, J. S. 1967 Salt fingers across a density interface. *Deep-Sea Res.* **14**, 599–611.

WALSH, D. & RUDDICK, B. R. 2000 Double-diffusive interleaving in the presence of turbulence: the effect of a non-constant flux ratio. *J. Phys. Oceanogr.* **30**, 2231–2245.